Synaptic properties and network state-dependent recruitment of VIP-expressing interneuron-specific interneurons in the CA1 hippocampus

Xiao Luo[1,2†], **Alexandre Guet-McCreight**[3,4†], **Ruggiero Francavilla**[1,2], **Vincent Villette**[1,2‡], **Frances K Skinner**[3,5], **Lisa Topolnik**[1,2*]

***For correspondence:** Lisa.Topolnik@bcm.ulaval.ca (LT)

[†]These authors contributed equally to this work

Present address: [‡]Institut de Biologie de l'École Normale Supérieure (IBENS), École Normale Supérieure, CNRS, INSERM, PSL Research University, 46 rue d'Ulm. 75005 Paris, France.

[1]Department of Biochemistry, Microbiology and Bio-informatics, Laval University, Québec, PQ, Canada; [2]Neuroscience Axis, CHU de Québec Research Center (CHUL), Québec, PQ, Canada; [3]Krembil Research Institute, University Health Network, Toronto, ON, Canada; [4]Department of Physiology, University of Toronto, Toronto, ON, Canada; [5]Departments of Medicine (Neurology) and Physiology, University of Toronto, Toronto, ON, Canada

Abstract In the hippocampus, a highly specialized population of vasoactive intestinal peptide-expressing interneuron-specific (IS) inhibitory cells coordinates the activity of GABAergic interneurons. While disinhibition may play a critical role in hippocampal learning, the synaptic properties and recruitment of IS cells remain unknown. Here, we found that the CA1 type 3 IS cells (IS3) receive excitatory inputs through the Schaffer collateral and the temporoammonic pathways with synapse-specific properties. The computational models predicted that these synaptic inputs could rhythmically drive the IS3 cell firing during theta oscillations and sharp-wave ripples. However, recordings in awake mice revealed a large variability in IS3 cell recruitment, with preferential recruitment of these cells in relation to theta-run epochs and silence during sharp-wave ripples. Taken together, these data indicate that, while synaptic properties of IS3 cells predict a particular output, additional factors may modulate the cell recruitment during different behavioral and network states.

Introduction

In the hippocampus, GABAergic interneurons coordinate the activity of principal cells (PCs) and are themselves controlled through a variety of local and long-range inhibitory mechanisms (***Chamberland and Topolnik, 2012***; ***Klausberger and Somogyi, 2008***). Interneuron-specific (IS) inhibitory interneurons play a unique role in this circuitry as they provide synaptic inhibition exclusively to GABAergic cells. Three distinct types of IS interneurons have been described in the CA1 hippocampus on the basis of their axonal projections and neurochemical features, with vasoactive intestinal peptide (VIP) being identified as a major IS cell marker (***Acsády et al., 1996a***,b; ***Gulyás et al., 1996***). These cells reside in different CA1 layers and may integrate major excitatory inputs converging onto the CA1 area, including the Schaffer collaterals (SC) from CA3 pyramidal cells, local axon collaterals from CA1 pyramidal cells, and the temporoammonic (TA) path afferents from the entorhinal cortex.

Integrated differentially by individual interneuron types (***Ali and Thomson, 1998***; ***Glickfeld and Scanziani, 2006***; ***Losonczy et al., 2002***; ***Pouille and Scanziani, 2004***), CA1 afferent inputs determine the cell type-specific contribution of a given interneuron type to ongoing network activity during specific behavioral states (***Katona et al., 2014***; ***Klausberger et al., 2003***; ***Lapray et al., 2012***; ***Varga et al., 2012***). However, the synaptic and integrative properties of the CA1 IS interneurons remain unknown.

The VIP/calretinin-co-expressing type 3 IS cells (IS3s) innervate preferentially the somatostatin-expressing (SOM+) oriens lacunosum-moleculare (OLM) interneurons (***Acsády et al., 1996b***; ***Chamberland et al., 2010***; ***Tyan et al., 2014***). Synchronous activation of IS3 cells is capable of coordinating the firing rate and timing of OLM interneurons (***Tyan et al., 2014***), which *in vivo* fire preferentially at the trough of theta oscillations and remain silent during sharp wave-associated ripples (SWRs) (***Katona et al., 2014***; ***Klausberger et al., 2003***; ***Lapray et al., 2012***; ***Varga et al., 2012***). While SOM+ OLM cells have been considered essential for generation of theta oscillations (***Gillies et al., 2002***; ***Gloveli et al., 2005***), selective manipulation with CA1 SOM+ interneuron population had almost no impact on the presence of intrinsic theta rhythm in the isolated hippocampus *in situ*. Yet, SOM+ interneurons were important in modulating the TA input integration by PCs (***Amilhon et al., 2015***). Moreover, silencing of CA1 SOM+ cells increased the burst firing of PCs (***Lovett-Barron et al., 2012***; ***Royer et al., 2012***) likely through facilitated integration of the SC and TA inputs (***Amilhon et al., 2015***; ***Lovett-Barron et al., 2014***). In addition to distal dendrites of PCs, OLM cells also target the local stratum radiatum (RAD) interneurons (***Leão et al., 2012***; ***Sik et al., 1995***). The OLM-to-interneuron circuit thus sub-serves a role in CA1 PC disinhibition that may facilitate selection of the intrahippocampal information and enhance the CA3 gating (***Leão et al., 2012***; ***Siwani et al., 2018***). Interestingly, recent modeling work has shown that the OLM-to-interneuron pathway is critical in producing a robust theta output in the isolated hippocampus (***Chatzikalymniou and Skinner, 2018***). Thus, IS3 cell input to SOM+ interneurons, and OLM cells in particular, may act as a higher-level control mechanism regulating the gating of the SC vs TA inputs in the CA1 area. Whether IS3 cells are recruited during *in vivo* theta oscillations and fire synchronously remains unknown. But if this is indeed the case, IS3 cells' role in the CA1 will be to pace the OLM cell activity for rhythmic gating of CA1 excitation during hippocampus-dependent learning.

In this study, we examined the synaptic and integrative properties of CA1 IS3 cells in hippocampal slices and investigated their contribution to network oscillations in awake mice. We found that IS3 cells can fire spikes in response to both the SC and TA input activation. Moreover, the TA-specific NMDA receptor expression may allow for the significant increase in the IS3 cell firing probability during repetitive TA activation. Integrating intrinsic and synaptic properties of IS3 cells into computational models and simulating an *in vivo*-like state, we could predict rhythmic IS3 cell recruitment during theta-oscillations and SWRs. However, *in vivo* Ca^{2+} imaging in awake mice showed variable recruitment of these cells during theta-oscillations and no correlation with SWRs recorded during immobility. Together, these results indicate that while IS3 cells are able to fire in response to both the SC and TA inputs and are preferentially activated during theta oscillations, additional factors may modulate their activity.

Results

Synaptic properties of IS3 interneurons

We took advantage of two transgenic mouse lines (*VIP-eGFP* and *VIP-Cre*) that express enhanced green fluorescent protein (*eGFP*) or Cre recombinase in VIP-expressing (VIP+) interneurons (***David and Topolnik, 2017***; ***Tyan et al., 2014***) (***Figure 1A***). The *VIP-Cre* mice were crossed with a reporter Ai9 line to achieve the *tdTomato* expression in VIP+ cells (***Madisen et al., 2010***). Consistent with previous findings on VIP expression in the hippocampal interneurons (***Acsády et al., 1996a***,b; ***Köhler, 1982***; ***Léránth et al., 1984***), in both mouse models, fluorescently-labeled cells were located throughout the CA1, with half of these having a vertical bipolar orientation that resembled the IS3 cell morphology

(***Figure 1A***) (***Tyan et al., 2014***). Indeed, 48.8% of VIP+ interneurons in the CA1 area (375/683 cells, n = 3 *VIP-eGFP* mice; 319/739 cells, n = 2 *VIP-tdTomato* mice) were co-expressing calretinin (CR) consistent with the IS3 neurochemical profile (***Acsády et al., 1996a***). The remainder were VIP+/CR- cells, including a sparsely distributed population of cholecystokinin-coexpressing (CCK+) basket cells (oriens/alveus: 15.2%, pyramidal layer: 10.2%, RAD: 25.8%, LM: 22.2% of total VIP+ interneuron number/layer; average data for two mouse lines; ***Figure 1***, ***Figure Supplement 1***). We characterized the morphological and electrophysiological properties of VIP+ cells by making targeted patch-clamp recordings from CA1 RAD VIP+ interneurons in slices from both mouse lines. All biocytin-filled VIP+ cells included in this analysis (n = 68) had soma located in the RAD, bipolar or monopolar dendrites extending to the LM and an axon arborizing within the oriens/alveus (***Figure 1B-C***), consistent with the IS3 cell morphology (***Acsády et al., 1996a***; ***Chamberland et al., 2010***; ***Tyan et al., 2014***). These cells had high input resistance (VIP-eGFP mouse line: 569 ± 38 MOhm; VIP-tdTomato mouse line: 505 ± 91 MOhm) and slow membrane time constant (VIP-eGFP: 25.5 ± 1.8 ms, VIP-tdTomato: 23.7 ± 1.3 ms; mean ± SEM here and in all subsequent text) (n = 19, ***Figure 1***, ***Figure Supplement 2C***). Depolarizing steps elicited slow action potentials (half-width, VIP-eGFP mouse line: 1.2 ± 0.06 ms; VIP-tdTomato mouse line: 1.3 ± 0.2 ms) with regularly spiking or stuttering firing pattern (***Figure 1***, ***Figure Supplement 2A–C***). The IS3 cell membrane and morphological properties were similar between the two mouse lines except the membrane capacitance, which was lower in VIP-tdTomato mice likely due to a smaller soma size (***Figure 1***, ***Figure Supplement 2***) (***David and Topolnik, 2017***; ***Tyan et al., 2014***). Therefore, both mouse models were used for studying the synaptic properties of IS3 cells.

Spontaneous excitatory synaptic drive was very low in these cells (***Figure 1D***). In voltage clamp recordings, spontaneous excitatory postsynaptic currents (EPSCs) acquired at -70 mV in the presence of gabazine had the average frequency of 0.07 ± 0.01 Hz and the average amplitude of 19.9 ± 2.5 pA (n = 6). In contrast, the frequency of spontaneous inhibitory postsynaptic currents (IPSCs) recorded at the reversal potential for EPSCs (0 mV) was significantly higher (1.64 ± 0.13 Hz, $p < 0.001$; ANOVA; average amplitude of IPSCs: 20.3 ± 2.8 pA, n = 6), indicating that under basal conditions in slices the IS3 cells receive a dominant inhibitory drive.

The laminar location of IS3 cell dendrites suggests that these cells may be preferentially driven via SC and TA inputs from CA3 pyramidal cells and entorhinal cortex, respectively. Accordingly, electrical stimulation in the RAD to activate the SC input elicited kinetically fast and large amplitude EPSCs in IS3 cells (amplitude = 24.0 ± 3.8 pA, rise time = 1.0 ± 0.3 ms, decay tau = 3.9 ± 1.0 ms, n = 9; ***Figure 1E-F***), which exhibited a linear current-voltage (I-V) relationship (***Figure 1F***), in line with a major role of the GluA2-containing Ca^{2+}-impermeable AMPARs at SC-IS3 cell synapses. In contrast to electrical stimulation within the RAD, stimulation within the LM to activate the TA input evoked slow, small amplitude EPSCs in IS3 cells (***Figure 1E,G***). Depolarizing the membrane above -50 mV revealed a second slow component to the TA-EPSC, indicating that NMDA receptors (NMDARs) may be present at TA-IS3 cell synapses. Indeed, the current-voltage relationship of the fast EPSC was linear whereas that of the slow component was outwardly rectifying (***Figure 1G***, n = 13), suggesting that NMDARs contribute to the TA path transmission onto IS3 cells. Blocking the AMPA receptors with NBQX (12.5 μM) removed the fast component (peak EPSC amplitude decrease to 13 ± 5% of control at -70 mV, n= 10; ***Figure 1H***), while application of AP5 (100 μM), an NMDAR antagonist, blocked the slow component of TA-EPSCs (peak EPSC amplitude decrease to 23.2 ± 5.9% of control at -30 mV). Together, these data point to the synapse-specific contribution of NMDARs in IS3 cells, in line with previous reports on the input-specific organization of excitation in other interneuron types (***Lei and McBain, 2002***; ***Le Roux et al., 2013***; ***Glickfeld and Scanziani, 2006***; ***Hainmüller et al., 2014***; ***Sambandan et al., 2010***).

We next explored the temporal and spatial integration of SC and TA inputs by IS3 cells using patch-clamp recordings, and electrical stimulation or two-photon glutamate uncaging. We found that both inputs show facilitation in response to repetitive stimulation at 10 to 40 Hz (***Figure 2A-C***). However, the facilitation degree at TA-IS3 synapses was significantly higher than that at SC-IS3

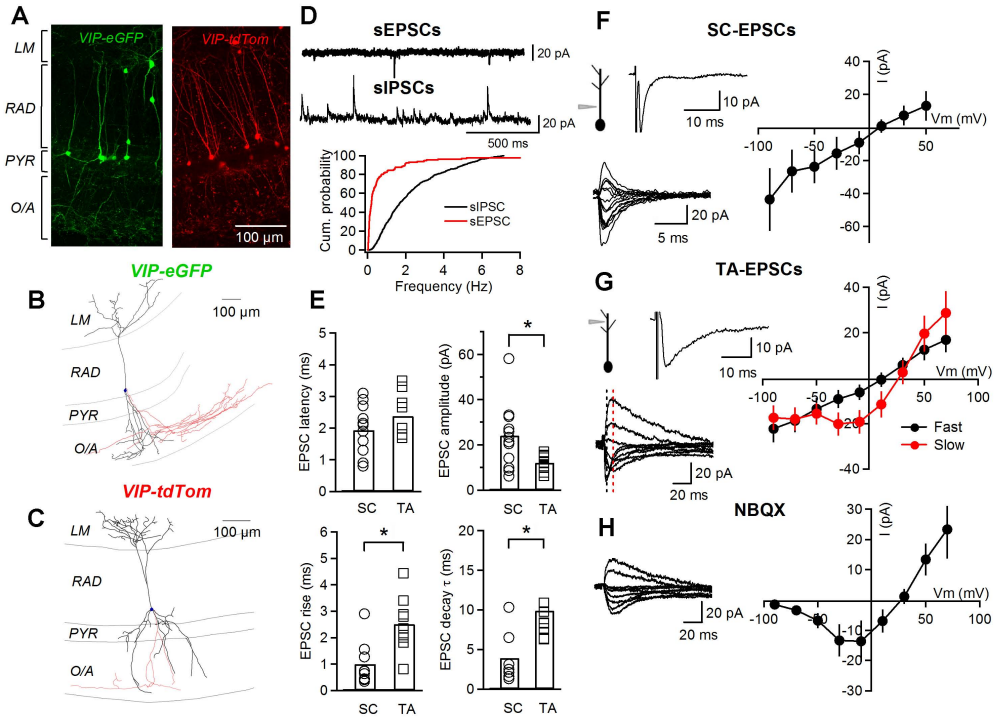

Figure 1. Properties of SC- and TA-EPSCs in IS3 cells. A: Two-photon images of CA1 area in slices from VIP-eGFP (green) and VIP-tdTomato (red) mice. **B-C:** Anatomical reconstructions of IS3 cells in VIP-eGFP (B) and VIP-tdTomato (C) mice. **D:** Examples of recordings of sEPSCS and sIPSCs (top) and a summary cumulative distribution for sEPSC and sIPSC frequency (bottom). **E:** Summary bar graphs showing the basic properties of SC-IS3 and TA-IS3 EPSCs. The individual data points (each point is a single cell) are shown for SC (circles) and TA (squares) EPSCs, respectively. The bars indicate the means (*: P<0.05, one-way ANOVA). **F:** Left top, schematics illustrating the location of the stimulation electrode for SC pathway activation and an example trace of SC-EPSC recorded at -70 mV. Left bottom, example traces of SC-EPSCs recorded at different voltage levels. Right, I-V curve of SC-EPSCs. **G:** Left bottom, schematics illustrating the location of stimulation for TA pathway and an example trace of TA-EPSC. Left bottom, example traces of TA-EPSCs obtained at different voltage levels. Black and red vertical dotted lines indicate the peak levels for fast and slow EPSC components, respectively. Right, I-V curves of TA-EPSC fast (black) and slow (red) components. **H:** Example traces of TA-EPSCs at different voltage levels (left) and an I-V curve (right) obtained in the presence of NBQX.

Figure 1–Figure supplement 1. Immunolabelling for CR and CCK in the CA1 hippocampal area of VIP-eGFP (green) and VIP-tdTomato (red) mice. A-B: GFP (green), CR (red) and CCK (red) immunoreactivity is shown overlayed. Insets in the lower right corner delineated by a white frame show examples of cells co-expressing GFP and CR (A) or GFP and CCK (B). **C-D:** tdTomato (red), CR (green) and CCK (green) immunolabelling overlayed. Insets in the lower right corner delineated by a white frame show examples of cells co-expressing tdTomato and CR (C) or tdTomato and CCK (D).

Figure 1–Figure supplement 2. Membrane and morphological properties of IS3 cells in VIP-eGFP (green) and VIP-tdTomato (red) mouse lines. **A-B:** Example traces of voltage responses (top) to depolarizing and hyperpolarizing current steps (bottom). **C:** Comparison of membrane properties and morphological parameters of IS3 cells in VIP-eGFP (green) and VIP-tdTomato (red) mouse lines.

inputs for all frequencies tested (10 Hz: $p < 0.05$; 20 Hz: $p < 0.01$; 40 Hz: $p < 0.01$; n = 18, one-way ANOVA). Indeed, compared with SC-EPSCs, TA-EPSCs increased stronger in response to trains of stimuli (5 pulses; 10 Hz: TA-EPSC5/EPSC1 ratio = 2.3 ± 0.08; SC-EPSC5/EPSC1 ratio= 1.6 ± 0.2; 20 Hz: TA-EPSC5/EPSC1 ratio = 2.6 ± 0.09; SC-EPSC5/EPSC1 ratio = 1.7 ± 0.1; 40 Hz: TA-EPSC5/EPSC1 ratio = 3.4 ± 0.1; SC-EPSC5/EPSC1 ratio = 1.8 ± 0.2; n = 18; ***Figure 2C***). These data indicate that both SC- and TA-IS3 cell synapses have a low release probability, with TA-IS3 input possessing a higher "detonating" capacity (***Silver, 2010***; ***Zucker and Regehr, 2002***). To examine the synapse-specific recruitment of IS3 cells, we combined current-clamp recordings with repetitive stimulation. At both SC-IS3 (n = 6) and TA-IS3 (n = 5) synapses, repetitive stimulation at 20-40 Hz resulted in strong summation of excitatory postsynaptic potentials (EPSPs) and increased cell firing, although activation of TA-IS3 synapses evoked significantly less of action potentials (APs) at 20 Hz (AP number; SC-IS3-20Hz: 8.7 ± 2, n = 5; TA-IS3-20Hz: 3.3 ± 0.7, n = 6; $p < 0.05$; SC-IS3-40Hz: 11 ± 3.1, n = 5; TA-IS3-40Hz: 8 ± 1.4, n = 6; $p > 0.05$; one-way ANOVA, ***Figure 2D***). These results indicate that IS3 cells can be driven via both SC and TA inputs during high frequency activity patterns, and that the CA3 input will be more efficient in recruiting these cells during lower activity levels.

What can be the minimal number of synapses that need to be activated to drive IS3 firing via SC vs TA inputs? To address this question, we used two-photon glutamate uncaging along the IS3 dendrite to mimic the activation of different number of excitatory synapses. As IS3 dendrites exhibit a very low density of spines, to estimate the synapse number activated in our experiments we considered as a reference point the average synapse density reported for dendrites of CR+ cells (RAD: 8.5-10 synapses/10 μm; LM: 7.5 synapses/10 μm) (***Gulyás et al., 1999***). In hippocampal slices from *VIP-eGFP* mice, two-photon uncaging (730 nm, 9 ms) of MNI-glutamate (5 mM) along the IS3 dendrite (2–8 μm length) elicited EPSPs (***Figure 2E-G***) that were completely abolished by the combination of AMPA and NMDA receptor antagonists (NBQX, 12.5 μM; AP5, 100 μM; n = 3, not shown). We then explored how many synapses were potentially required for triggering APs at SC vs TA inputs by uncaging glutamate on proximal (SC input, < 50 μm from the soma, n = 6) vs distal (TA input, > 100 μm from the soma, n = 5) dendritic segments of increasing length. The data showed that at segments receiving SC and TA synapses APs can be evoked within the same dendritic length (SC-IS3: 6.5 ± 0.1 μm; ***Figure 2F,H***; TA-IS3: 5.1 ± 0.1 μm; ***Figure 2G,H***; $p > 0.05$, unpaired t-test). We performed simple approximations of the number of synapses necessary for AP generation using the anatomical data for CR+ dendrites of ***Gulyás et al.*** (***1999***). We could predict that, although the dendritic lengths that were triggering a single AP at SC- vs TA-IS3 synapses were similar, the number of synapses activated could slightly differ due to the dendrite-specific synapse densities (SC-IS3: 5-7 synapses; TA-IS3: 4-5 synapses) (***Gulyás et al., 1999***). Collectively, these results indicate that, when activated synchronously, clusters of ~5 synapses at different dendritic locations should be able to drive the IS3 cell firing.

Synaptic properties of IS3 cells predict that they fire during rising/peak phases of theta oscillations and during SWRs *in vivo*

We then took advantage of our previous IS3 cell multi-compartment models (***Guet-McCreight et al., 2016***) developed in the NEURON software environment (***Carnevale and Hines, 2006***) to predict input-specific synaptic recruitment of IS3 cells. Using SC- and TA-EPSCs, we fit the weights, rise times, and decay times for excitatory synapses (reversal potential = 0 mV) onto each dendritic compartment of the model. We took the synaptic weights from the best fit on the proximal dendrites and the best fit on the distal dendrites, and extrapolated to obtain a linear distance-dependent weight rule. All synapses on the proximal and distal dendrites were then also assigned the rise and decay times of their corresponding best fits. We did a similar process for inhibitory synapses (reversal potential = -70 mV), where we fit the synaptic parameters to a spontaneous IPSC (amplitude: 20.3 ± 2.8 pA; rise time: 0.52 ± 0.07 ms; decay time: 2.8 ± 0.5; n = 6). Here we extrapolated a linear distance-dependent weight rule according to the weights of the two most optimal fits, and fixed the time constants according to the time constants of the most optimal fit (***Guet-McCreight et al., 2017***). Altogether,

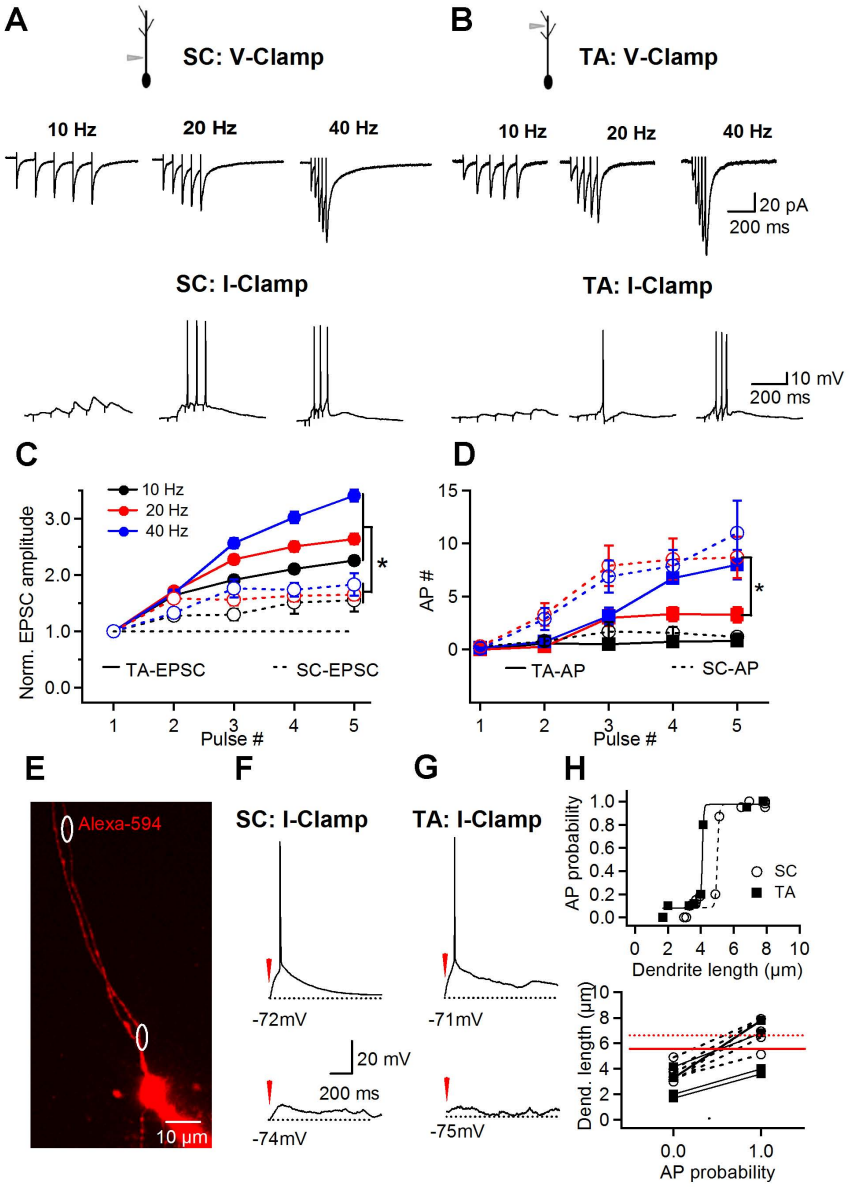

Figure 2. Input-specific temporal and spatial summation. **A:** Schematics illustrating the stimulating electrode location for the SC pathway activation (upper), and the example traces in response to repetitive stimulation (10, 20 and 40 Hz) in voltage (middle) and current (bottom) clamp mode. **B:** Same as panel A for TA-stimulation. **C:** Normalized EPSC amplitudes in response to repetitive stimulation of SC vs TA inputs. Solid lines and closed symbols indicate TA-EPSC, dashed lines and open symbols indicate SC-EPSC (*: P<0.05, one-way ANOVA. The EPSCs induced by the last three pulses were compared between TA and SC pathway). **D:** The average number of APs generated in response to different stimulation frequencies at TA vs SC synapses. The statistical analysis was performed on the APs induced by the fifth pulse at 20Hz. (*: P<0.05, one-way ANOVA). **E:** Two-photon image (single focal plane) showing the IS3 cell filled with Alexa-594 during recording and the location of the target areas in proximal (SC) and distal (TA) dendrites for two-photon glutamate uncaging; **F-G:** Representative responses of IS3s when glutamate was released at shorter (bottom, 2-4 μm) and longer dendritic areas (top, 5-8 μm) at SC (F) vs TA (G) inputs. **H:** Top, representative example of the AP probability in relation to photostimulation extend at two inputs. Bottom, summary data for a group of cells illustrating the transition to AP initiation when the length of stimulated dendrite was increased. Circles correspond to the SC and squares - to the TA inputs, respectively. Red lines indicate the mean threshold for dendritic length, at which it was possible to induce spikes at SC (dotted line) vs TA (continuous line) inputs. The difference in the dendritic length was not significant between the two inputs. P > 0.05; Mann-Whitney test.

these extrapolations generated realistic EPSCs and IPSCs across the entire dendritic arbor of the IS3 cell model from the soma to the distal dendrites (***Figure 3***). The weights used here predicted a biologically realistic range of receptors per synapse (***Figure 3***, ***Figure Supplement 1A***). The model also predicted an increase in the measured reversal potential with distance from soma (***Figure 3***, ***Figure Supplement 1B1***), which is in line with what was seen experimentally due to the signal decay from the synapse on the dendrite to the soma (***Figure 1F-G***; ***Figure 3***, ***Figure Supplement 1B2***).

We next used these realistic synaptic parameters (***Guet-McCreight et al., 2017***) to simulate *in vivo*-like conditions in our IS3 cell model (***Guet-McCreight and Skinner, 2018***), where the model was bombarded with synaptic inputs. In our computational explorations, we tested two IS3 cell model variants that did (SDprox1) or did not (SDprox2) have dendritic A-type potassium channels (***Guet-McCreight et al., 2016***). Using our baseline *in vivo*-like models, we applied theta- and SWR-timed inputs to examine when IS3 cells are likely to be recruited to spike *in vivo*.

For theta-timed inputs in an *in vivo*-like scenario (***Figure 4***), we assumed phasic excitatory and inhibitory inputs that only spiked once per cycle (***Figure 4A3***), with a small amount of noise in their exact timing since this was found to enhance model recruitment during theta-timed inputs (***Figure 4***, ***Figure Supplement 2***). We included different proximal and distal dendritic excitatory and inhibitory populations based on the relative timing of different hippocampal populations during theta (***Mizuseki et al., 2009***; ***Klausberger and Somogyi, 2008***) (***Figure 4A1-A2***). We found that both CA3 and EC inputs could mediate the phasic timing of IS3 cell recruitment (***Figure 4B–D***), with EC inputs driving the model to fire during the rising phase of theta, and CA3 inputs driving the model to fire near the peak of theta (***Figure 4***, ***Figure Supplement 1*** and ***Figure Supplement 2***). Considering various proximal and distal inhibitory inputs at several phases of theta (i.e. the peak, the falling phase, and the trough), we found that inhibitory inputs mostly reduced spike recruitment during theta (***Figure 4***, ***Figure Supplement 1***). This was likely due to there being too many inhibitory inputs as this effect was pronounced when any of the inhibitory input subgroup numbers were doubled (***Figure 4***, ***Figure Supplement 1C-D)***. In other words, significant inhibition could counteract excitatory inputs and thus reduce recruitment during theta. Notably though, this effect was seen less with inhibitory inputs occurring near the falling phase and the trough. Overall, these results suggest that IS3 cells would spike near the rising phase and peak of a theta cycle *in vivo* (***Figure 4***), and that their recruitment is driven by excitatory inputs arriving near the rising phase and peak (***Figure 4***, ***Figure Supplement 1***). It also predicts that inhibitory inputs near the falling phase and trough will modulate IS3 recruitment during theta, but that too much inhibition will counteract IS3 cell recruitment.

Considering SWR-timed inputs in an *in vivo*-like scenario (i.e. transient inputs that last for 50 ms) (***Katona et al., 2014***; ***Varga et al., 2014***), we first looked at proximal excitatory inputs alone with a burst frequency mimicking CA3 PCs (***Frerking et al., 2005***) (***Figure 5A–B***, left). We found that IS3 cells could exhibit an increase in activity above baseline when receiving CA3 inputs alone (***Figure 5C-D***). We then included a delayed feed-forward inhibitory input onto the proximal dendrites with a frequency that could correspond to bistratified (BIS) cell spiking (***Katona et al., 2014***) (***Figure 5B***, center). In increasing the number of SWR-timed inhibitory inputs we found a substantial reduction in spike recruitment (***Figure 5C–D***, center). Finally, we also included a delayed feed-forward inhibitory input onto the distal dendrites with a frequency that could correspond to OLM cell spiking (***Katona et al., 2014***). This did not generally show much more of a decrease in activity back to baseline (***Figure 5C–D***, right). Note that the SDprox1 and SDprox2 models showed similar results and re-randomizing the synapse locations and presynaptic spike times also showed similar results (***Figure 5C-D***). From the simulations done for ***Figure 4*** and ***Figure 5***, we did not observe any consequential differences between our two model variants (SDprox1 and SDprox2) with theta and SWR timed recruitment. This could be because the addition of synaptic inputs needed to generate baseline *in vivo*-like electrophysiological outputs was dependent on the model variant (***Guet-McCreight and Skinner, 2018***). Thus this lack of difference in recruitment cannot be directly explained by the inclusion (SDprox1) or exclusion (SDprox2) of dendritic A-type potassium channels. Taken together, these results suggest that IS3 cells could spike during SWRs upon receiving CA3 input. However, the

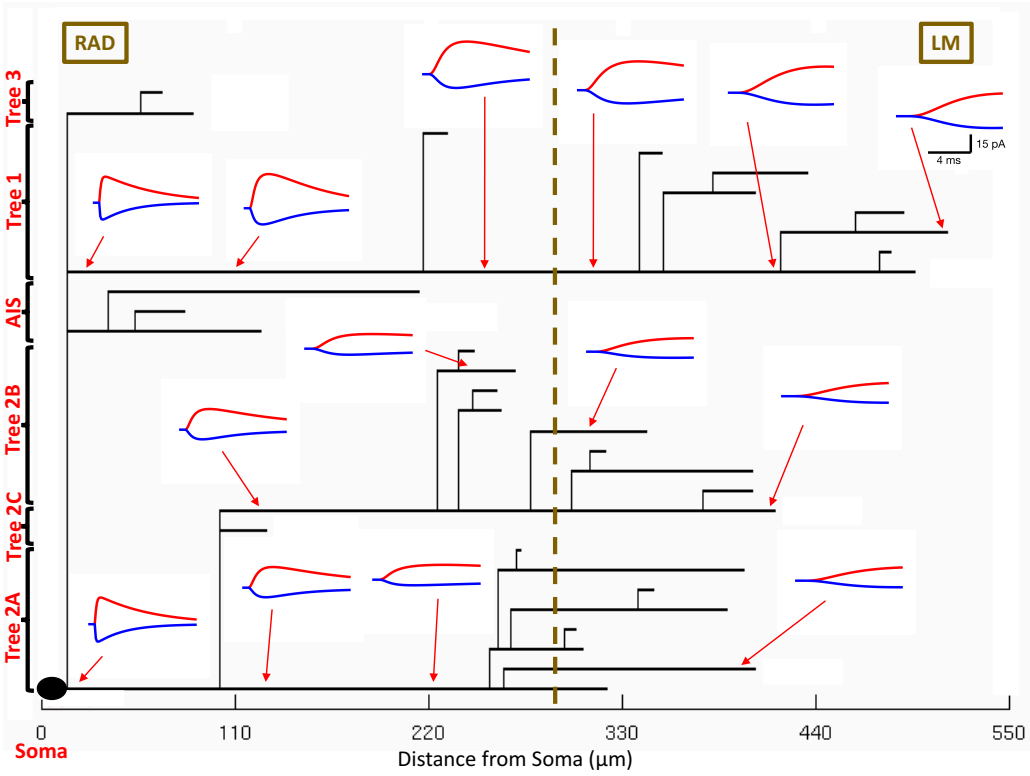

Figure 3. EPSCs and IPSCs along model dendritic tree. Simulated somatically-recorded EPSCs (blue) and IPSCs (red) generated from synapses at selected locations along the dendritic arbor of the IS3 cell model (i.e. with linearly rectified weights). Note that both the IPSCs and EPSCs exhibit a waveform broadening and amplitude deterioration with synaptic distance from soma. Red arrows denote the approximate synaptic locations. Dashed brown line shows the border between proximal and distal dendrites at 300 μm from the soma. Labels on the y-axis denote the dendritic subtree labels. RAD = Stratum Radiatum; LM = Stratum Lacunosum Moleculare; AIS = axon initial segment.

Figure 3–Figure supplement 1. Receptor numbers, reversal potentials and electrotonic distances. A: Predicted ranges of receptors per synapse, calculated based on the fitted weights (blue) and the linearly rectified distance-dependent weights (red). Note that each x-axis data point shows a range which is larger or smaller depending on the thickness (along the y-axis) of the plotted line. Dashed red line denotes the maximal limits as per previous findings from other cell types in the literature. Line bifurcations in this plot correspond to bifurcations in the dendritic morphology. **B1:** Estimated reversal potential of each synapse along the dendritic arbor of the model using a simulated protocol that is similar to what is used experimentally. Note that the true reversal potential of each excitatory synapse is 0 mV, and does not change during these simulations. Line bifurcations in this plot correspond to bifurcations in the dendritic morphology. **B2:** Electrotonic distance (i.e. decay of a 1 mV signal) for voltage flowing into the soma (left) and voltage flowing out of the soma (right). Note that the subtree organization approximately follows the same organization as in B1, suggesting that reversal potential recordings in IS3 cells are sensitive to distance-dependent voltage decay.

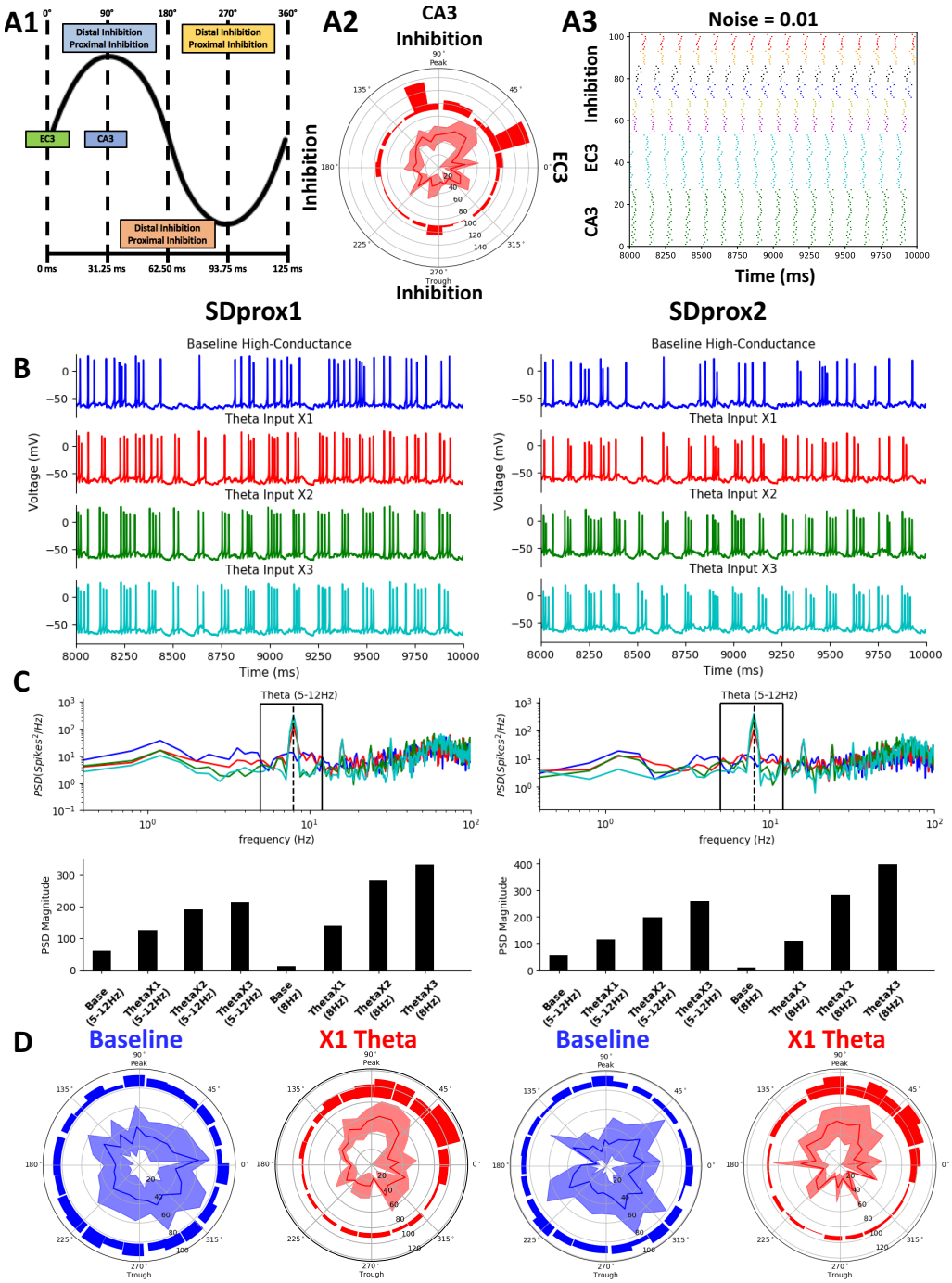

Figure 4. Recruitment of IS3 cell models with theta-timed inputs. A1: Relative timing of different theta-timed presynaptic populations. **A2:** Same as A1, but in polar plot format with an example plot of SDprox1 phase preference when theta-inputs are perfectly timed. **A3:** Example raster plot of the presynaptic theta-timed populations. **B:** Example simulated SDprox1 and SDprox2 voltage traces of resulting baseline *in vivo*-like conditions, X1 theta inputs, X2 theta inputs and X3 theta inputs. **C:** Top subplot: Power spectral density (PSD) of the SDprox1 and SDprox2 IS3 cell model spike trains during baseline *in vivo*-like conditions, X1 theta inputs, X2 theta inputs, and X3 theta inputs. Bottom subplot: first four bars show the area under the PSD between 5-12 Hz, and the last four bars show the PSD magnitude at 8 Hz. **D:** Polar plots showing phase preference of the SDprox1 and SDprox2 IS3 cell models. Inner traces show the mean frequencies of the interspike intervals, binned according to phase (binned standard deviations shown in the shaded areas). Outer histograms show the binned spike phases (bin width = 14.4°).

Figure 4–Figure supplement 1. Excitatory presynaptic populations can modulate timing of IS3 cell spikes during theta rhythms. A1-B1: Same as in *Figure 4C* for X1 theta-timed inputs, but during removal of specified presynaptic theta-timed populations. Bottom subplots show only the PSD at 8 Hz. **A2-B2:** Same as in the *Figure 4D* theta polar plots (bin width = 14.4°), but during removal of either CA3 or EC3. **C-D:** Same as in A-B, but with doubled presynaptic populations instead of removed. Acronyms: CA3 - Cornu Ammonis 3, EC3 - Entorhinal Cortex Layer 3, SR90/180/270 - Theta Peak/Falling Phase/Trough -Timed Proximal Inhibition, SLM90/180/270 - Theta Peak/Falling Phase/Trough -Timed Distal Inhibition.

Figure 4–Figure supplement 2. Effect of fractional randomness (noise) on theta-recruitment in the SD-prox1 model. **A:** Example X1 theta raster plots of the presynaptic theta-timed populations. **B:** Same as in *Figure 4C*. **C-E:** Polar plots (same as in *Figure 4D*) showing phase preference of the IS3 cell model for X1 (C), X2 (D), and X3 (E) theta inputs (bin width = 14.4°).

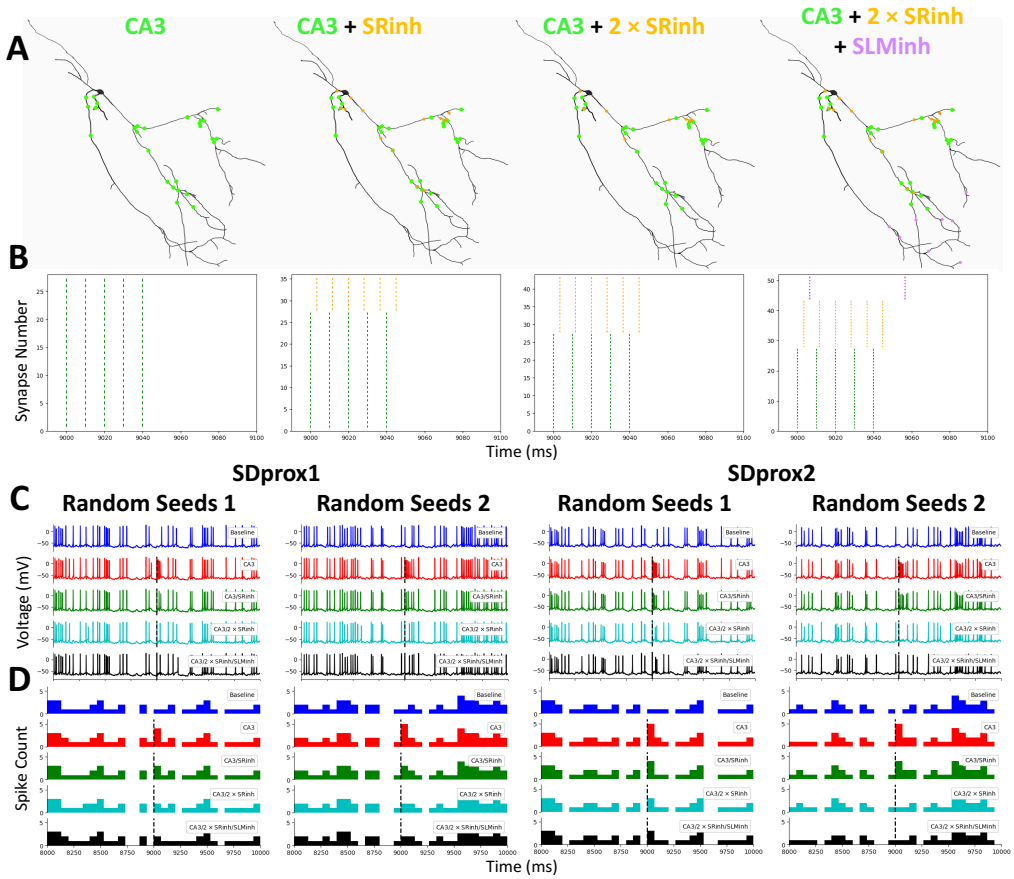

Figure 5. Recruitment of IS3 cell models with SWRs. A: Example synaptic locations of SWR-timed inputs. Note that synaptic locations are chosen randomly in all simulations. **B:** Raster plots of SWR-timed presynaptic populations. **C:** Example voltage traces during SWR-timed inputs. Dashed black line coincides with the start of the SWR event. Note that we show two examples for both SDprox1 and SDprox2 where we resample synaptic locations and baseline presynaptic spike times. **D:** Example peri-stimulus histogram of the voltage traces shown in C (bin size is 67ms - 30 bins). Results show that delayed proximal inhibition is sufficient to bring the model spiking back to baseline levels. Acronyms: CA3 - Cornu Ammonis 3, SRinh - Proximal Feedforward Inhibition, SLMinh - Distal Feedforward Inhibition.

presence of feed-forward proximal inhibitory SWR-correlated inputs (e.g. from BIS cells or possibly other VIP+ or CR+ interneuron types) would have a strong dampening effect on IS3 cell SWR-recruitment. Thus, IS3 cells can be silenced during SWRs depending on the excitatory/inhibitory input balance.

Recruitment of IS3 cells in awake mice

To test the model predictions, we next examined the recruitment of IS3 cells during different brain states *in vivo* using two-photon calcium imaging in awake, head-restrained mice trained to run on the treadmill (***Villette et al., 2017***). To express the genetically-encoded calcium indicator GCaMP6f (***Chen et al., 2013***) in VIP+ cells for calcium imaging *in vivo*, a Cre-dependent viral vector AAV1.Syn.Flex.GCaMP6f.WPRE.SV40 was injected into the CA1 area of *VIP-Cre* mice (n = 3 mice). Two-photon somatic calcium imaging was performed within the hippocampal CA1 PYR and RAD, where most IS3 cells are located (***Figure 1****A*; ***Figure 1***, ***Figure Supplement 1***; ***Figure 6****C*). This was combined with local field potential (LFP) recordings from the contralateral CA1 area, as well as recordings of the animal's speed (***Figure 6****A-B*). In this simple behavioral paradigm the animals can voluntarily alternate between immobility (speed < 1 cm/s), and locomotion (speed > 1 cm/s; ***Figure 6****B*), allowing us to record and analyze hippocampal theta oscillations during locomotion and SWRs during quiet states (***Figure 6****D-E*). To separate IS3 cells from VIP+ basket cells (BCs), we first developed a set of morphological criteria based on the soma properties derived from the anatomically reconstructed neurons recorded *in vitro* and identified as IS3 cells or BCs (***Figure 6***, ***Figure Supplement 1****A1-B1*; IS3: n = 36; BC: n = 11). The 3D rendering of somatic surface was used to develop the soma areas and extract the soma diameters in medio-lateral X- and rostro-caudal Y-dimensions (***Figure 6***, ***Figure Supplement 1****A2-A3,B2-B3*). Similarly, the X- and Y- parameters corresponding to different soma diameters were extracted from VIP+ cells imaged *in vivo* (***Figure 6***, ***Figure Supplement 1****D1-D2,E1-E2*). Based on the data distribution for soma diameter and area in anatomically confirmed IS3 cells and VIP+ BCs recorded *in vitro* (***Figure 6***, ***Figure Supplement 1****C*), the cut-off parameters ($X \leq 16$ μm, $Y \leq 11$ μm, soma area size ≤ 152 μm^2) were established to separate putative IS3 cells (pIS3) from the putative BCs (pBC) imaged *in vivo* (***Figure 6***, ***Figure Supplement 1****F*; pIS3 n = 9; pBC, n = 12). To validate the appropriateness of the selected cut-off parameters for identification of the *in vivo* recorded VIP+ cells, following *in vivo* imaging, the mouse brains were processed for immunolabelling for GFP and CR, the IS3 cell marker (***Figure 6***, ***Figure Supplement 1****G*). The results showed that CR- (pBC) and CR+ (pIS3) cells in PYR/RAD separate well into two clusters using our cut-off criteria (***Figure 6***, ***Figure Supplement 1****H*; CR+: n = 17; CR-: n = 13).

Using the established morphological criteria for pIS3 cell separation, we then explored pIS3 cell activity during locomotion and immobility (n = 18 cells, 221 running periods and 556 stationary states from 2 imaging sessions of 5 min each). *Post hoc* immunohistochemical analysis of recorded neurons (2 out of 18 VIP+ PYR/RAD interneurons recorded *in vivo* were found after brain re-sectioning and processed for CR) confirmed that VIP+ cells identified as pIS3 were positive for CR (2 cells out of 2 tested; ***Figure 6****F*). To analyze calcium transients during run epochs (***Figure 7****A*), we identified periods in the speed traces of > 1 cm/s that lasted for at least 3 consecutive seconds. We then further selected run epochs that were preceded by 5 seconds of average speed below 1 cm/s (i.e. run-starts; 64 epochs selected across 17/18 cells) or followed by 5 seconds of average speed below 1 cm/s (i.e. run-stops; 69 epochs selected across 18/18 cells; ***Figure 7****B*). In correspondence with run epochs, there was an increase in the time-varying max theta power (***Figure 7****C*). In looking at the mean calcium responses across the pIS3 cells, we mainly observed calcium transients during run-stop periods (***Figure 7****D*), pointing to the delayed recruitment of pIS3 cells during theta-run epochs. The timing of this change was so variable across different pIS3s, however, that it was imperceptible when looking only at the median of mean calcium traces across run epochs (***Figure 7****D*, black line).

We also calculated cross-correlations between calcium signals and running speed or the time-varying theta power (***Figure 7****E-F*). Specifically we looked at whether each set of time series were significantly cross-correlated in time by looking at their cross-correlation magnitudes at lags of zero

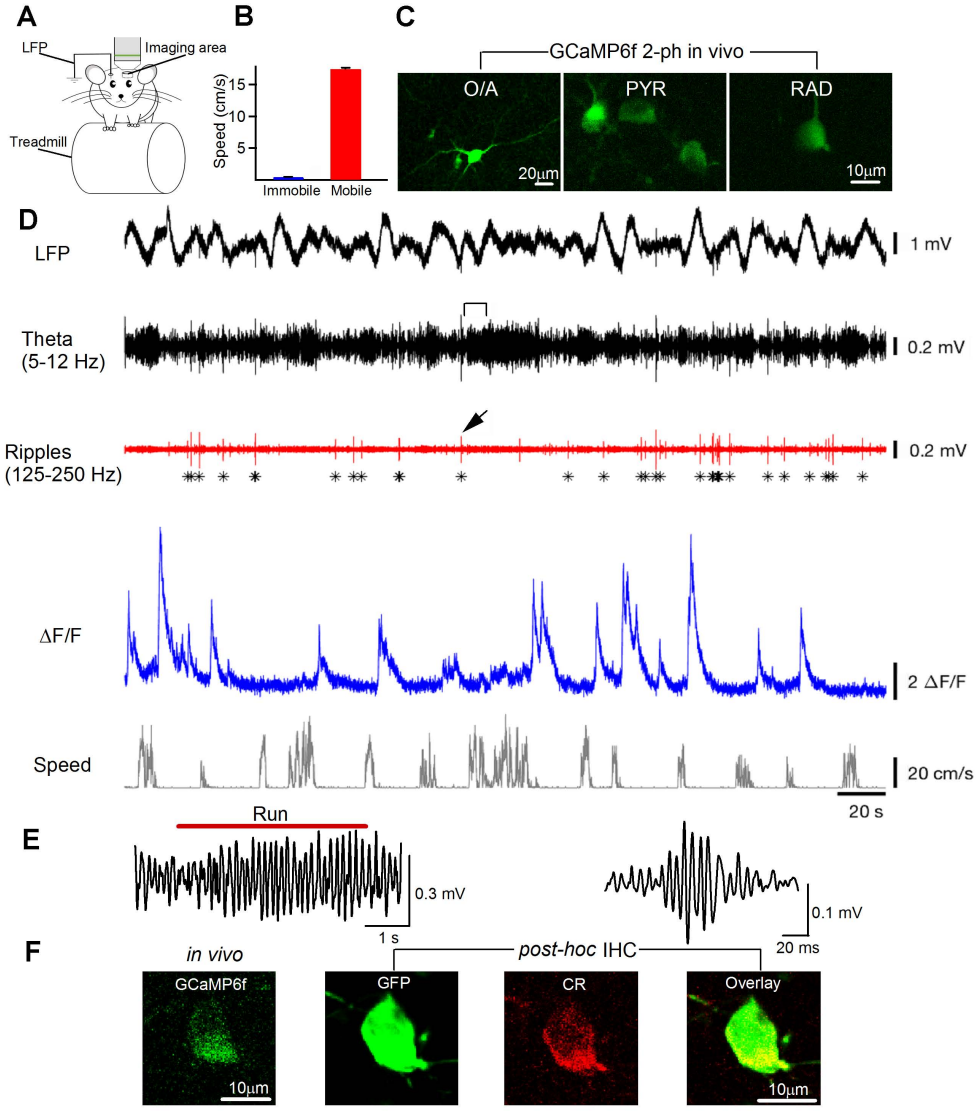

Figure 6. Imaging activity of pIS3 cells in awake mice. A: Schematic of simultaneous calcium imaging and LFP recordings in awake mice. **B:** Bar graph showing the average running speed during different behavioral states. **C:** Representative two-photon images showing VIP+ cells located within O/A, PYR and RAD. Note a smaller size round soma of VIP+ cells within PYR and RAD. **D:** Representative traces of simultaneous LFP recording [from top to bottom, raw trace and filtered for theta: 5–12 Hz (black) or ripples: 125-250 Hz (red, with black stars showing individual ripple episodes)] and somatic calcium transients (blue) from a pIS3 cell during different behavioural states (grey trace: the higher animal speed during locomotion is reported as a high-frequency step pattern). The *post hoc* identification of this cell as CR+ is illustrated in F. **E:** Left, expanded theta-run period indicated by bracket in D (red line indicates the duration of the running period). Right, expanded ripple event indicated by an arrow in D. **F:** Left, two-photon image showing an IS3 soma labeled with GCaMP6f and recorded *in vivo*. Right, *post hoc* verification of CR expression in the same cell.

Figure 6–Figure supplement 1. Morphological criteria used for the VIP cell identification. A-B: Neurolucida 3D reconstructions (A1, B1) and confocal images (A2-A3, B2-B3; maximal projections of 10–32 sections) illustrating the analysis of somatic parameters in anatomically confirmed IS3 cells and BCs filled during in vitro patch-clamp recordings with biocytin. 3D rendering of somatic surface (A2, B2) was used to derive somatic diameters in medio-lateral (X-axis) and rostro-caudal (Y-axis) dimensions (A3, B3). **C:** Summary bar graphs illustrating the distributions of somatic diameters in a group of cells (IS3, blue, n = 36; BC, black, n = 11). **D-E:** Two-photon raw (D1, E1) and mask (D2, E2) images of VIP interneurons recorded in vivo showing the extraction of somatic X- and Y-parameters for cell identification. **F:** Summary data showing the clustering of in vivo recorded VIP cells based on the distribution of X- and Y-parameters (pIS3, blue, n = 9; pBC, black, n = 12). Dotted lines indicate the cut-off levels obtained from in vitro analysis and used for in vivo cell segregation (X = 15.9 µm, Y = 11.3 µm). **G**: Representative confocal images of horizontal hippocampal sections processed for post hoc immunohistochemical identification following in vivo two-photon experiments illustrating the expression of GFP (G1), CR (G2) and both (G3). **H:** Summary group data showing the clustering of CR+ and CR- VIP cells based on the distribution of X- and Y-parameters (pIS3, blue, n = 17; pBC, black, n = 13). Dotted lines indicate the same cut-off levels.

seconds (i.e. zeroth peaks) as well as their maximal peak magnitudes and corresponding lag times (***Figure 7***, ***Figure Supplement 1****A-D*, see methods). Significant zeroth peaks indicated that events (e.g. run epochs and calcium transients) from the two time series co-occurred in time. The lag time of the maximal peaks (i.e. if the maximal peak magnitude was significant) indicated the approximate delay with which the events from one signal lagged behind the events from another signal. Specifically, if maximal peak lag times were negative, this indicated that calcium transients followed run-theta epochs (and the opposite if positive). For both speed and theta power, we found that almost all cells had significant zeroth peaks and maximal peaks (***Figure 7***, ***Figure Supplement 1****A-D*). Most cells (N = 15/18 for speed; N = 15/18 for theta power) also had slightly negative (i.e. -5s to 0s) maximal peak lag times. This indicated that calcium transients occurred with a slight delay relative to run-theta epochs. In fact, this can be seen in the example shown in ***Figure 6****D*, as well as the general observation that calcium transients tended to occur around run-stop periods (***Figure 7****D*).

As well, we computed Pearson's correlations between speed and calcium traces or estimated spike rate traces from three different spike estimation algorithms (see next section). We obtained significant relationships between speed and the calcium signal across all pIS3 cells, though different cells varied in whether this relationship was positive, negative, or flat (***Figure 7****G*). The variability in the sign of these relationships is at least partly due to variability in cross-correlation lag times between signals (i.e. see ***Figure 7***, ***Figure Supplement 1****A-D*). For example, larger negative lag times between speed traces and calcium signals meant that calcium transients were occurring closer to periods of immobility following run epochs, which meant more negative relationships. Also, relationships between speed and estimated spike rates were not always significant, but there was consistency of whether the relationship was positive or negative for the different spike estimation algorithms. Similarly, Pearson's correlations between time-varying theta power and calcium traces or estimated spike rate traces equally showed consistently similar results when compared to the Pearson's correlations for speed (***Figure 7***, ***Figure Supplement 1****E*). Together, we conclude that the activity of pIS3 cells correlates with running speed and theta oscillation power, however they exhibit a delayed recruitment.

IS3 cells prefer to fire near the rising/peak phases of theta oscillations

To further examine pIS3 activites during different network states and test model predictions, we used several methods to estimate spike times from GCaMP6f calcium signals. This included the Matlab toolboxes MLspike (***Deneux et al., 2016***) and UFARSA (***Rahmati et al., 2018***), as well as custom Matlab code for estimating spike times using the gradient of the calcium signal (DF/Dt; similar to what was used in ***Jackson et al.*** (***2016***)).

Across the spike times estimated from all methods (***Figure 8****A*), we observed a larger mean

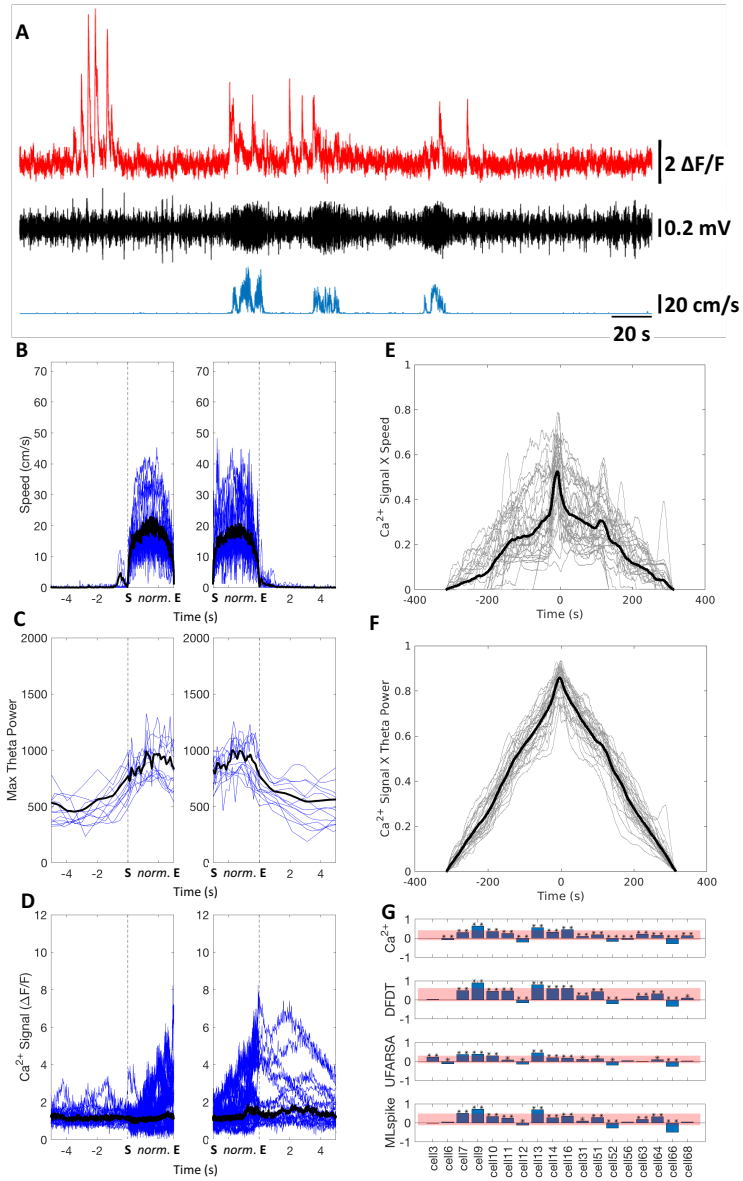

Figure 7. Delayed recruitment of pIS3 cells during theta-run epochs. A: Representative simultaneously recorded traces of a calcium signal from a pIS3 cell (red), a theta-filtered (5-12Hz) LFP recording (black), and animal speed (blue trace). **B-D:** Average traces of speed (B), theta power (C), and calcium activity (D) during run-starts (left panels; averages are across 64 run-starts selected across 17/18 cells) and run-stops (right panels; averages are across 69 run-stops selected across 18/18 cells). The vertical dashed lines show the transition into (left panels) or out of (right panels) run epochs. "S" denotes the start time of a run epoch, and "E" denotes the end time of a run epoch. For the run epoch portions in the time axes, the time vector is normalized (i.e. by using Matlab's `interp1(___)` function) such that the run epochs occupy the same span across the x-axis, despite having variable durations. The times outside of these run epochs are shown normally (i.e. ±5s pre- and post- run epochs). Blue lines show the mean traces for each cell. The mean of means across cells are shown in black, except for the calcium signal in D, which shows the median of means. **E-F:** Cross-correlations between the calcium signal and speed (E), and the time-varying theta power (F). Average traces across all recordings are shown in black, and individual session traces are shown in grey. Speed cross-correlations (E) were quite variable but generally tended to exhibit large peaks near zero. Theta-filtered cross-correlations (F) also exhibited a mean large peak near zero. **G:** Pearson correlations of speed with either calcium signal magnitude (top subplot), DF/Dt estimated spike rates (upper middle subplot), UFARSA estimated spike rates (lower middle subplot), or MLspike estimated spike rates (bottom subplot; * < 0.05; ** < 0.001). Red area indicates the mean ± standard deviation.

Figure 7–Figure supplement 1. Summary statistics of cross-correlations and Pearson correlations between theta power and calcium signal. A-B: Analysis of speed x calcium signal cross-correlations (for raw traces, see ***Figure 7E***). Dots indicate the lag time of the maximum peaks versus the magnitude of the maximum (A) or zeroth (B) peaks seen in the cross-correlations. Histograms along the ordinate axes show the distributions of cross-correlation maximum peak amplitudes and zeroth peak amplitudes. The color of dots indicates the significance of the cross-correlation using a 10s structured reshuffling surrogate analysis. Black dots indicate p-value > 0.05, blue dots indicate p-value < 0.05, and red dots indicate p-value < 0.01. **C-D:** Same as A-B but for analysis of theta power x calcium signal cross-correlations (for raw traces, see ***Figure 7F***). **E:** Same as in ***Figure 7G*** but with time-varying theta power instead of speed.

normalized percent of spikes during locomotion compared to immobility, as shown in DF/Dt and MLspike methods (***Figure 8B***), indicating an overall higher activity of pIS3s during locomotion. However, some cells exhibited a larger normalized percent of spikes during immobility (3/18 cells), indicating that this state-dependent preference was variable across the cells (***Figure 8B***).

We then analyzed the theta phasic distributions of spikes where the speed was greater than 1 cm/s and the time-varying theta power was greater than its mean (i.e. periods of running and high-theta activity). In pooling all of the spike phases across cells into a single distribution for each method (***Figure 8C***), we observed significant non-uniform distributions ($p < 0.001$, Rayleigh's Tests), and significant polarities towards the circular means across all spike phases (***Table 1***; $p < 0.001$, V-Tests). However, these distributions also exhibited large amounts of dispersion. To characterize this dispersion, we looked at vector length and angular deviation. Vector lengths closer to 1 indicate more clustering of angles around the mean (i.e. less dispersion) and larger angular deviation values (with a maximum possible value of 81.03) indicate larger amounts of dispersion. We found vector lengths much smaller than 1 (***Table 1***) and angular deviations close to the maximal possible value of 81.03°(***Table 1***), which indicates broad distributions of spikes across theta phases.

To further investigate this result, we performed second-order analyses in which the mean of the mean angles across all the cells was examined using the three spike estimation methods. We found significant mean spike phase preferences with most vector lengths towards the rising/peak phase of the theta cycle ($p < 0.05$, Rayleigh's Test; $p < 0.01$, V-Test; ***Figure 8D***), indicating that IS3 cells may be preferentially recruited during this phase of the theta oscillation. In comparing the three methods, we note that in the mean of means analyses, the UFARSA method generated the largest amount of phasic dispersion, that is, a large variability. Specifically, several of the cells exhibited large vector lengths towards the falling phase and trough of theta (***Figure 8D***, middle). This can be explained by noticing that the individual UFARSA spike phase histograms (not shown) for some particular cells (i.e. cells #6, #11, #13, and #51) possessed low spike number estimates during running/high theta (i.e. 4, 4, 16, and 9 spikes, respectively) relative to the other two methods. This is possibly due to the UFARSA method underestimating the number of spikes compared to the other two methods. Low estimates using the UFARSA method was not limited to these particular cells, as two other cells (cells #12 and #52) were found to not have any spikes during periods of running and high theta. It is possible that the low spike number estimates with the UFARSA method increased the probability of outliers. Another outlier of note was the large vector length of 1 seen for one of the cells in the DF/Dt mean-of-means polar plot (***Figure 8D***, left). Upon closer inspection, this cell (i.e. cell #12) was found to have only one DF/Dt spike estimated during running/high theta, thus explaining why it generated a vector length of 1 (i.e. meaning no phasic dispersion).

IS3 cells are silent during ripples

We did not observe any apparent calcium transients that coincided with ripple activity (***Figure 9A***), indicating that pIS3 cells are likely silent during ripples. Indeed, using DF/Dt and MLspike algorithms, we extracted a few spikes co-localized in time with ripples (***Figure 9B***), which represented a small proportion of the total number of spikes. As well, in looking at the peri-stimulus time histograms of estimated spiking relative to sharp-wave ripple occurrence, we did not observe any increase in spike

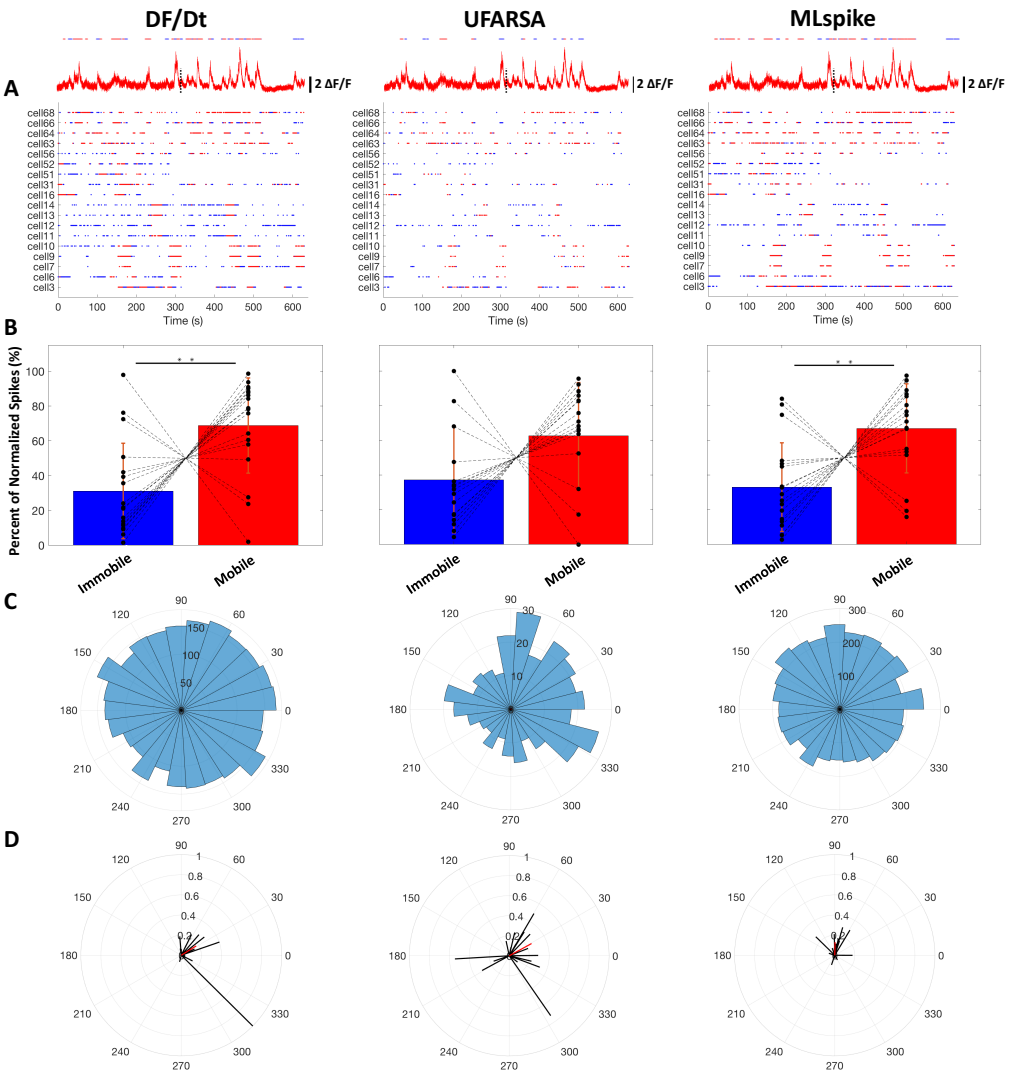

Figure 8. Estimations of spike times from calcium signals suggest spike preferences during movement and near the rising/peak phases of theta, with a high degree of spike phase dispersion. Three different methods were used: DF/Dt, UFARSA, and MLspike. **A:** Raster plots for each cell, where blue dots are estimated spikes during immobile states, and red dots are estimated spikes during mobile states. Above each of the raster plots is a calcium trace from cell #66, above which are the estimated spike extractions using each method. The dashed line in the calcium traces indicates the time point where there was a 1 min break between recording sessions. **B:** Percent of spikes for each state normalized relative to the states where the animal was spending most of their time (statistical significance across states was evaluated using paired-sample t-tests). The dashed lines indicate which data points belong to the same cell (black dots). Bars indicate the mean, and the error bars indicate the standard deviation. Statistical significance is indicated by "*" (*$p < 0.05$, **$p < 0.01$, ***$p < 0.001$). **C:** Pooled distribution of spike phases (i.e. across all cells) relative to the theta-filtered LFP, where spike count is shown on the radial axis (bin width = 14.4°). These pooled distributions were significantly non-uniform (Rayleigh's test), with significant non-uniform polarities (v-test) towards the circular means of the distributions (see ***Table 1***). **D:** Mean of means test. Each line shows the mean spike phase preference of a cell along the polar axis, where the vector length is shown along the radial axis. The red lines indicate the mean of means angles (i.e. polar axis) and the mean vector lengths (i.e. radial axis). Again, these were significantly non-uniform (Rayleigh's test), with significant non-uniform polarities (V-Test) towards the circular mean of the means (see ***Table 1***).

Table 1. Circular Statistical Tests.

Pooled Spike Phases	**DF/Dt**	**UFARSA**	**MLspike**
Mean Angle	39.18	34.68	77.99
Vector Length	0.07	0.17	0.09
Angular Deviation	78.21	73.91	77.15
Rayleigh's Test (P-Value)	4.10e-8	6.94e-6	1.21e-19
Rayleigh's Test (Z-Stat)	16.99	11.81	43.47
V-Test (P-Value)	2.78e-9	5.88e-7	0
V-Test (V-Stat)	248.38	70.34	465.54
Mean of Means	**DF/Dt**	**UFARSA**	**MLspike**
Mean of Mean Angles	32.08	28.66	88.75
Mean of Vector Lengths	0.17	0.25	0.13
Angular Deviation of Means	52.31	61.03	59.51
Rayleigh's Test (P-Value)	1.45e-3	0.03	0.02
Rayleigh's Test (Z-Stat)	6.12	3.37	3.82
V-Test (P-Value)	2.33e-4	4.72e-3	2.85e-3
V-Test (V-Stat)	10.50	7.79	8.29

probability density during ripples (***Figure 9****B*, top subplots). This suggests that IS3 cells are silent during SWRs despite the model predictions. In fact, as the model suggests, they can be silenced through activation of different inhibitoty inputs (***Figure 5****C–D*, center), though these predictions remain to be examined in detail.

Discussion

Here, we demonstrate that IS3 cells receive TA and SC excitatory inputs with input-specific glutamate receptor composition and spatio-temporal integration properties. In particular, TA-IS3 synapses express NMDA receptors postsynaptically and show a larger degree of short-term facilitation during repetitive synaptic activity compared to that of SC-IS3 synapses. Despite a different dendritic location, both TA and SC-IS3 synapses were able to drive the IS3 cell spiking when a cluster of at least five closely spaced inputs was activated synchronously. Furthermore, model simulations predicted that the synaptic properties of IS3 cells allow them to fire during rising/peak phases of theta oscillations and during SWRs in simulated *in vivo*-like conditions. The recruitment of these cells during theta oscillations was controlled through rhythmic excitatory inputs from the CA3, EC3, and local inhibitory populations. Moreover, the CA3 and EC3 inputs provided the largest degree of modulation in terms of the firing timing of IS3 cells. During SWRs, the model predicted that CA3 input alone would be sufficient to recruit these cells. However, experimental data using two-photon calcium imaging of pIS3 cells in awake mice revealed a large degree of variability in their activity. Moreover, they exhibited delayed recruitment during theta-run epochs and were silent during SWRs. Consistent with the model predictions, however, the activity of pIS3 cells correlated well with theta power and animal speed, and they could preferentially fire during the rising/peak phases of theta-run episodes. Taken together, these data indicate that additional local and long-range synaptic mechanisms may modulate the recruitment of IS3 cells during different behavior and network states.

The TA vs SC pathway-specific properties of excitatory synaptic transmission have been well characterized in PCs (***Otmakhova et al., 2002***; ***Arrigoni and Greene, 2004***). Compared with the SC-PC synapses, TA-PC input exhibits slow kinetics and a larger NMDA/AMPA receptor ratio (***Otmakhova et al., 2002***). In hippocampal interneurons, the distribution and subunit composition of ionotropic glutamate receptors is input- and cell type-specific. This has a profound impact on the input

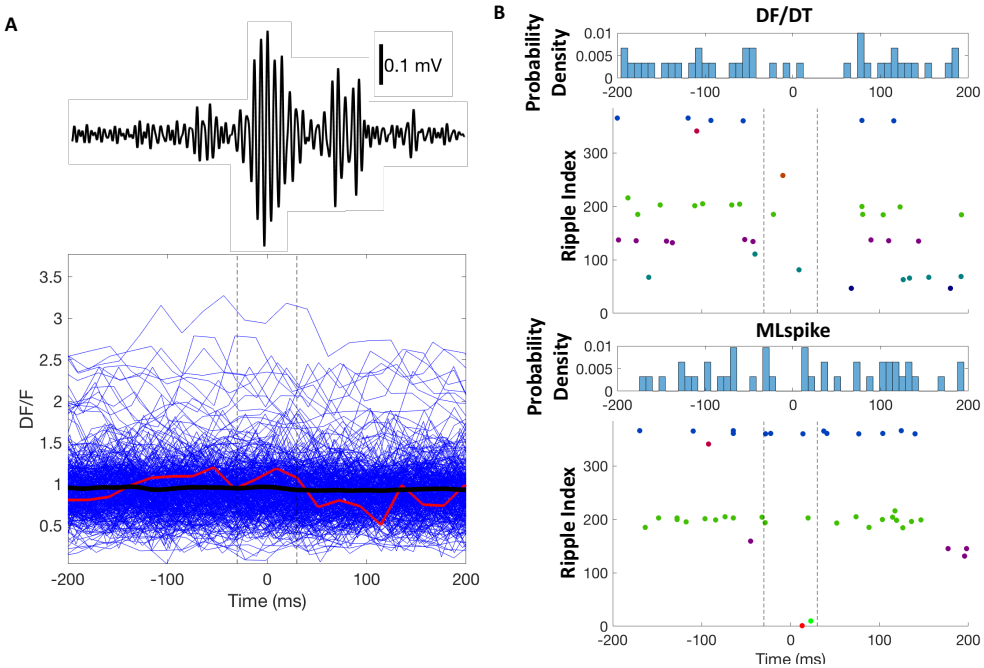

Figure 9. pIS3 cells are not activated during SWRs. A: Peri-stimulus time histogram of all calcium traces (blue lines) that occur during SWRs. The red line shows the calcium trace that corresponds to the example SWR shown above the plot. The black line shows the mean across all calcium traces. The dashed lines highlight the ±30ms time window surrounding the SWR, which is centered at 0ms along the time axis. **B:** Peri-stimulus time histogram of the spike times estimated from the MLspike and DF/Dt algorithms. Note that UFARSA is not shown since only two estimated spikes occurred within this ±200ms time window (i.e. across all ripples observed), and both of these spikes were not within the ±30ms time window of any ripple. Note that the ripple index on the y-axis highlights how many ripples were analyzed, and the different dot colors corresponds to estimated spike times estimated from different cells. Bin size in top subplots is 8 ms (i.e. 50 bins).

integration and induction of synaptic plasticity (**Nyíri et al., 2003**; **Lamsa et al., 2007**; **Croce et al., 2010**; **Szabo et al., 2012**). Specifically, the excitatory synaptic transmission at TA and SC pathways was compared in neurogliaform cells (**Price et al., 2005**), and NMDA and AMPA receptors were found to be present at both pathways. Our data indicate that TA-IS3 EPSCs in IS3 cells have slower kinetics than those evoked at the SC synapses, which in addition to dendritic filtering, can be explained in part by contribution of the NMDA receptors. The I-V curves for the fast component of both TA- and SC-EPSCs showed linear relationships, indicating the involvement of the Glu2A-containing AMPA receptors. These data are consistent with the transcriptomic analysis of excitatory inputs' composition in VIP+ neocortical interneurons (**Paul et al., 2017**). In particular, the *Gria2* (GluR2 subunit) mRNAs were highly enriched in VIP+/CR+ neocortical interneurons. In addition, the *Grin2b* (GluN2B subunit) transcripts were preferentially expressed in VIP+/CR+ cells. The larger NMDA/AMPA receptor ratio at distal dendrites may have impact on dendritic integration and induction of synaptic plasticity in IS3 cells, such that the slow kinetics of the TA-EPSC may provide a longer time window for excitatory input integration, along with the induction of Hebbian LTP (**Regehr and Tank, 1990**; **Golding et al., 2002**; **Dudman et al., 2007**; **Kullmann and Lamsa, 2007**). In addition, NMDAR spikes generated at distal dendrites have been shown to facilitate AP firing and the induction of associative LTP in PCs (**Brandalise et al., 2016**). Whether these mechanisms may operate in interneurons, and in IS3 cells in particular, remains to be examined.

Similarly, the short-term plasticity at excitatory synapses in hippocampal interneurons displays afferent and cell type-specific features (**Thomson, 1997**; **Ali et al., 1998**; **Sun et al., 2005**; **Croce et al., 2010**). Such complexity in input processing might arise from the highly variable pre- and post-synaptic distribution of ionotropic and metabotropic glutamate receptors (**Shigemoto et al., 1996**; **Sun and Dobrunz, 2006**; **Chittajallu et al., 2017**). The fact that IS3 cells exhibited exclusively short-term facilitation at both inputs may imply similar presynaptic mechanisms operating at the SC- and TA-IS3 synapses with low initial release probability (**Katz and Miledi, 1968**). In addition, a larger facilitation at TA-IS3 synapses may involve the NMDA receptors, especially if it contains the kinetically slow GluN2B-subunit (**Chamberlain et al., 2008**).

Furthermore, our data showed that it is likely that a similar number of synchronously activated synapses in proximal or distal dendrites were required for eliciting the AP firing of IS3 cells. It has been documented that the density of excitatory synapses on thick proximal dendrites of CR+ cell is 85.36/100 μm (0.85/μm) while on distal dendrites it is 75.31/100 μm (0.75/μm) (**Gulyás et al., 1999**). Accordingly, based on the dendritic length required to evoke a single AP in different dendritic domains (proximal: 6.5 μm, distal: 5.1 μm), the minimal number of synapses leading to AP generation may correspond to $\sim$5 on proximal and $\sim$4 synapses on distal dendrites. This observation indicates that additional mechanisms, such as increased NMDA/AMPA receptor ratio at distal dendrites (**Otmakhova et al., 2002**), synaptic scaling of AMPA receptors (**Magee and Cook, 2000**) or dendrite site-specific distribution of potassium channels in IS3 cells (**Guet-McCreight et al., 2016**) may compensate for dendritic filtering (**Stuart and Spruston, 1998**; **Emri et al., 2001**).

How can these synaptic mechanisms control IS3 cell recruitment *in vivo*? Using computational simulations, we demonstrate the impact of different excitatory and inhibitory inputs on IS3 cell firing. First, we note that the relative timing and level of activity along the CA3 and EC pathways can modulate the timing of IS3 cell recruitment during theta. If both were to strongly influence IS3 cell spiking, this could enhance the variability of cell recruitment during theta rhythms. Second, removing inhibition occurring at the falling phase and trough of theta oscillation could increase the spike initiation, pointing to the importance for these phase-specific inputs in IS3 cell recruitment during theta. However, doubling inhibition would decrease IS3 cell firing, regardless of the phase, which indicates that too much inhibition can hinder recruitment of these cells. This suggests that during theta, IS3 cells are likely modulated through specific local and long-range GABAergic projections. Specific timing and levels of inhibition provided by these inputs may be responsible for delayed recruitment of IS3 cells during theta-run epochs. The candidate local inhibitory inputs that could fit the spatio-temporal patterns of theta activation shown here include OLM, bistratified,

basket, and neurogliaform cells (***Mizuseki et al., 2009***; ***Klausberger and Somogyi, 2008***), although it is still unknown whether they are connected to IS3 cells. It is also possible that IS3 cells receive inputs from IS1 and IS2 cells (though the timing of these cells during theta remains unknown), as well as the medial septum (MS) GABAergic projections. The morphological studies showed that long-projecting MS GABAergic neurons make multiple synaptic contacts with hippocampal VIP+ cells (***Papp et al., 1999***), raising the possibility that they may also play a role in modulating IS3 cells during network oscillations (***Dragoi et al., 1999***; ***Hangya et al., 2009***; ***Viney et al., 2013***; ***Unal et al., 2015***). Furthermore, in line with model predictions, the *in vivo* calcium imaging of pIS3 cells with estimated spike times demonstrated that these cells appear to preferentially fire during the rising/peak phases of theta, though with a large degree of phasic dispersion. The large variability in the experimental data relative to the model could be due to a number of factors including errors in spike time estimation by the different methods, impact of additional excitatory inputs that were not included in the model (e.g. from local CA1 PYR and subcortical neuronal populations), or cellular diversity within the pIS3 cell population (***Francavilla et al., 2018***), which remain to be explored in details.

The model also predicted that IS3 cells would spike during SWRs since they receive excitatory input from CA3 PCs. However, the presence of feed-forward inhibition could dampen the IS3 cell recruitment considerably. Indeed, in the *in vivo* calcium imaging experiments, we did not observe any correlation between the IS3 cell activity and SWR appearance. In addition to the feed-forward inhibition, this can be explained by the impact of subcortical neuromodulatory inputs, for example serotonergic projections from the median raphe nucleus (***Papp et al., 1999***) that can modulate hippocampal theta (***Prisco et al., 2002***; ***Domonkos et al., 2016***) and ripple (***Wang et al., 2015***) oscillations via specific cellular mechanisms due to the cell type-specific expression of different types of 5-HT receptors (***Freund et al., 1990***; ***Helboe et al., 2015***; ***Wyskiel and Andrade, 2016***). Whether the IS3 cells are targeted by these long-range projections and can be modulated during theta oscillations or ripples remains to be explored.

In conclusion, our data indicate that IS3 cell operation and function may be more complex than can be predicted from their synaptic properties. And, in agreement with previous observations on VIP+ interneurons in cortical circuits, these cells may be tuned by specific activity patterns and learning paradigms in relation to mood state and animal experience. For example, in the auditory cortex, VIP+ cells are strongly recruited by positive or negative reinforcement stimuli during auditory discrimination tasks (***Pi et al., 2013***). In the prefrontal cortex, the activation of VIP+ cells is coupled with the outcome of goal-directed behavior (***Pinto and Dan, 2015***). These data point to the role of modulatory systems in controlling the cortical disinhibition mediated by VIP+ cells. Thus, we cannot exclude that hippocampal IS3 cells can be preferentially involved in learning and memory-related behaviors and exhibit variable recruitment under basal conditions, such as our behavior paradigm.

Methods and Materials

Animals

Four mouse lines of both sex were used in this study: VIP/enhanced green fluorescent protein (VIP-eGFP), VIP-IRES-Cre (Jackson #010908), ROSA9 and VIP-IRES-Cre-ROSA9. VIP-eGFP line [MMRRC strain #31009, STOCK Tg(Vip-EGFP) 37Gsat] was purchased from the MMRRC facility at the University of California, Davis, CA, in which eGFP was targeted selectively to VIP+ interneurons (***Tyan et al., 2014***). VIP-tdTomato line was generated by breeding VIP-Cre mice with the reporter line Ai9-(RCL-tdTomato) (B6.Cg-Gt(ROSA)26Sortm9(CAG-tdTomato)Hze/J, stock #007909, The Jackson Laboratory). All experiments were performed in accordance with animal welfare guidelines of the Animal Protection Committee of Université Laval and the Canadian Council on Animal Care. Animals were housed in groups of 2–4 per cage with standard light/dark cycle and ad libitum access to food and water.

Whole cell patch-clamp recordings in hippocampal slices *in vitro*

Slices were prepared from P14-30 mice. Mice were deeply anaesthetized with isoflurane or ketamine-xylazine (10 mg/ml-1mg/ml). Mice older than P25 were intracardially perfused with ice cold artificial cerebrospinal fluid (ACSF) sucrose solution containing the following (in mM): 250 sucrose, 2 KCl, 1.25 NaH_2PO_4, 26 $NaHCO_3$, 7 $MgSO_4$, 0.5 $CaCl_2$, and 10 glucose (290-310 mOsm/L), oxygenated constantly with 95% O_2 and 5% CO_2, to improve the quality of acute brain slices. Transversal hippocampal slices were obtained with a vibratome (VT1000S; Leica Microsystems or Microm; Fisher Scientific) in ice cold ASCF sucrose solution and transferred to the recovery solution maintained at 37.5°C, containing (in mM): 124 NaCl, 2.5 KCl, 1.25 NaH_2PO_4, 26 $NaHCO_3$, 3 $MgSO_4$, 1 $CaCl_2$, and 10 glucose, oxygenated constantly with 95% O_2 and 5% CO_2 (290-310 mOsm/L).

After 1 hour of recovery, slices were transferred to the recording chamber and continuously perfused with ACSF solution containing (in mM): 124 NaCl, 2.5 KCl, 1.25 NaH_2PO_4, 26 $NaHCO_3$, 2 $MgSO_4$, 2 $CaCl_2$, and 10 glucose; 290-310 mOsm/L, which were oxygenated constantly with 95% O_2 and 5% CO_2. eGFP cells and tdTomato cells were identified with blue light and green light illumination, respectively, using upright microscope (Nikon Eclipse FN1), and visualized with differential interference contrast during patch-clamp recordings. Two-photon images of eGFP and tdTomato cells in acute slices were acquired with a 25x water-immersion objective (NA 0.95, 2.5 mm working distance) using a two-photon microscope (TCS SP5; Leica Microsystems) with Ti-sapphire laser (Chameleon Ultra II; Coherent; > 3W, 140 fs pulses, 80 Hz repetition rate) and laser wavelength tuned to 800 or 950 nm, respectively. For electrical stimulation, a theta glass pipette (Sutter instrument) was placed at *stratum lacunosum moleculare* or *stratum radiatum*. Borosilicate glass capillaries (World precision Instruments Inc.) were used to make patch pipettes for whole-cell recordings (tip resistance, 3–6 MΩ). For voltage-clamp recordings, the pipette was filled with a Cs-based solution (in mM): 130 $CsMeSO_4$, 2CsCl, 10 diNa-phosphocreatine, 10 HEPES, 4 ATP-Tris, 0.4 GTP-Tris, 0.3% biocytin, 2 QX-314, 0.1 spermine, pH 7.2–7.3, 280–290 mOsm/L. For current-clamp recordings, a K+-based intracellular solution was used, containing (in mM):130 $KMeSO_4$, 2 $MgCl_2$, 10 diNa-phosphocreatine, 10 HEPES, 4 ATP-Tris, 0.4 GTP-Tris and 0.3% biocytin (Sigma), pH 7.2–7.3, 280–290 mOsm/L. Passive membrane properties were recorded immediately after cell membrane rupture, active membrane properties were recorded in current-clamp mode in response to somatic current steps (from -200 to +800 pA). Pharmacological experiments were performed in voltage-clamp mode at the holding potential of -70 mV. The following pharmacological agents were used: gabazine (10 μM, Ascent Scientific), CGP-55845 (2 μM, Abcam Biochemicals), NBQX (12.5 μM, Abcam Biochemicals) and D,L-AP5 (50 μM, Abcam Biochemicals). Gabazine and CGP-55845 were applied into the bath 10 min before electrical or optical stimulations to block the GABAergic transmissions. The EPSCs were evoked by electrical stimulation (1-5 pulses, 5-40 Hz, pulse width 0.2 ms) every 30 seconds. The series resistance (Rser) was monitored throughout the experiment by applying a -5 mV voltage step at the end of each sweep. Recordings with changes in Rser> 15% were discarded from the analysis. Data acquisition (filtered at 2-3 kHz and digitized at 10kHz; Digidata 1440, Molecular Devices, CA, USA) was performed using the Multiclamp 700B amplifier and the Clampex 10.5 software (Molecular Devices).

Two-photon glutamate uncaging

The protocol for two-photon glutamate uncaging was previously described in details (***Chamberland et al., 2010***). The Alexa Fluor 594 (20 μM) was included in the intracellular solution to visualize the cell morphology. The caged compound MNI-Glu (5 mM; Tocris) was introduced in the recording chamber and focal photolysis was performed by illuminating the proximal (<50 μm from soma) or distal (>100 μm from soma) dendritic segments of different length (2-8 μm) for 9 ms (the smallest photostimulation duration that can be achieved in xyt-mode with our two-photon system) with a 730-nm laser pulse (laser power, 25–30 mW, Leica TCS SP5 microscope with a 40×, 0.8 NA water-immersion objective; Leica Microsystems). The size of the uncaging region was increased gradually until an action potential was evoked. Two-photon images for dendritic visualization were acquired

using two-photon excitation at 800 nm (laser power 5-10 mW). To avoid photodamage, the uncaging-based stimulation was performed every 30 seconds, and the laser power did not exceed 40 mW. Uncaging-evoked EPSPs or action potentials were recorded in current clamp mode.

Computational model

Model Details and Code

The models used in this study were previously custom-built to simulate electrophysiological characteristics of IS3 cells (***Guet-McCreight et al., 2016***) (ModelDB accession #: 223031). Models were simulated in the NEURON software environment (***Carnevale and Hines, 2006***) and results were plotted using customized Python and Matlab scripts. Note that all code and scripts can be accessed online (synaptic optimization code: https://github.com/FKSkinnerLab/IS3-Cell-Model/tree/master/LayerSpecificInputTests; rhythmic input simulations code: https://github.com/FKSkinnerLab/IS3-Cell-Model/tree/master/RhythmTests).

Model Synapse Details

For the synapse model, we used NEURON's built-in Exp2Syn function, which models synaptic current as a two-state kinetic scheme.

$$i = G(V - E) \tag{1}$$

$$G = weight \times factor \times \left(exp\left(-\frac{t}{\tau_d} \right) - exp\left(-\frac{t}{\tau_r} \right) \right) \tag{2}$$

Where *i* is the synaptic current, *G* is the synaptic conductance, *E* is the reversal potential, *V* is the membrane potential, *weight* is the synaptic weight, *factor* is a NEURON process that is used to normalize the peak synaptic conductance to the value of weight, *t* is time, τ_r is the rise time, and τ_d is the decay time.

We used NEURON's Praxis Optimizer, to fit the synaptic parameters for each compartment to an experimental EPSC or IPSC. Excitatory synapses less than 300 μm from soma were fit to a SC-evoked EPSC, and excitatory synapses greater than 300 μm from soma were fit to a TA-evoked EPSC. All inhibitory synapses were fit to a spontaneous IPSC. We set the *weight*, τ_r, and τ_d, as the free parameters in the optimization and assumed that all voltage-gated channels were blocked since sodium and potassium channel blockers were used during the experimental recordings. To remove any driving forces caused by leak conductances, we also set the leak reversal potential to the voltage-clamped holding potential of the model (0 mV when fitting IPSC recordings, and -70 mV when fitting to EPSC recordings). During the optimizations, we used experimental τ_r and τ_d individual trace measurements as seed values (IPSC: = 0.25 ms and τ_d = 4.14 ms; $EPSC_{Proximal}$: τ_r = 0.45 ms and = 1.41 ms; $EPSC_{Distal}$: τ_r = 1.71 ms; τ_d = 5.04 ms) and used parameter bounds based on literature values (AMPA: ***Swanson et al.*** (***1997***); ***Masugi-Tokita et al.*** (***2007***); ***Antal et al.*** (***2008***); ***Nusser*** (***1999***); ***Spruston et al.*** (***1995***); ***Andrásfalvy and Magee*** (***2001***); ***Andersen et al.*** (***2006***); GABAA: ***Andersen et al.*** (***2006***); ***Ernst et al.*** (***2003***); ***Nusser et al.*** (***1997***); ***Nusser*** (***1999***)). These chosen parameter ranges and bounds were the following:

AMPA:
E_{rev} = 0 mV
τ_r = 0 ms to 5 ms
τ_d = 0 ms to 20 ms
$weight_{AMPAmax} = AMPA_{UnitaryConductance} \times AMPA_{MaxNumber}$
$weight_{AMPAmax} = 30pS \times 200receptors = 0.006\mu S$
$weight_{AMPA}$ = 0 to 0.012 μS (i.e. $weight_{AMPAmax} \times 2$)

GABAA:
E_{rev} = -70 mV

τ_r = 0 ms to 5 ms
τ_d = 0 ms to 50 ms
$weight_{GABAAmax} = GABAA_{UnitaryConductance} \times GABAA_{MaxNumber}$
$weight_{GABAAmax} = 30pS \times 500receptors = 0.015\mu S$
$weight_{GABAA}$ = 0 to 0.03 μS (i.e. $weight_{GABAAmax} \times 2$)
Presynaptic Spike Time = 0 to 6 ms

Using the weight value obtained from the most optimal fit for proximal dendritic synapses as well as the weight value obtained from the most optimal fit for distal dendritic synapses, we applied a linear distance-dependent weight rule for AMPA synapses:

$$weight_{AMPA} = (2.308 \times 10^{-6}\mu S/\mu m) \times Distance + (220.2 \times 10^{-6}\mu S) \quad (3)$$

Similarly, using the weight values obtained from the two most optimal fits for inhibitory synapses, we applied a linear distance-dependent weight rule for GABA$_A$ synapses:

$$weight_{GABAA} = (4.691 \times 10^{-6}\mu S/\mu m) \times Distance + (269.6 \times 10^{-6}\mu S) \quad (4)$$

Respectively, the rise times and decay times of all the excitatory synapses were fixed to the rise and decay times of their corresponding layer-specific most optimal fit. The rise times and decay times of all the inhibitory synapses were fixed to the rise and decay times of the most optimal inhibitory fit. **Excitatory SR**: τ_r = 2.9936 × 10^{-4} ms, τ_d = 2.4216 ms; **Excitatory SLM**: τ_r = 6.1871 × 10^{-4} ms, τ_d = 3.1975 ms; **Inhibitory**: τ_r = 0.1013 ms, τ_d = 4.8216 ms.

To get the ranges of numbers of receptors per synapse for each synaptic location (***Figure 3***, ***Figure Supplement 1A***), we computed the following:

$$(Receptors_{min}, Receptors_{max}) = Weight/(UnitaryConductance_{max}, UnitaryConductance_{min}) \quad (5)$$

To simulate the experimental protocol for estimating the distance-dependent reversal potential of each excitatory synapse (***Figure 3***, ***Figure Supplement 1B***), we held the soma in voltage-clamp mode and incrementally increased the holding potential. The reversal potential of each synapse was recorded as the holding potential when the polarity of the postsynaptic current at the soma reversed.

Baseline *in vivo*-Like Inputs

In vivo-like excitatory and inhibitory inputs (i.e. spike rates and numbers of active synapses) were estimated previously (***Guet-McCreight and Skinner, 2018***). In all simulations, the baseline *in vivo*-like synaptic locations and presynaptic spike trains were chosen randomly according to a set of random seeds. For SDprox1, baseline *in vivo*-like inputs have the following parameters: 144 excitatory synapses with 5 Hz rates each, and 8 inhibitory synapses with 50 Hz rates each. For SDprox2, baseline *in vivo*-like inputs have the following parameters: 144 excitatory synapses with 5 Hz rates each, and 24 inhibitory synapses with 10 Hz rates each.

Theta-Timed and SWR-Timed Inputs

Note that in all *in vivo*-like simulations, all synaptic locations (i.e. for baseline, theta-timed, and SWR-timed synapses) were chosen randomly such that synapses were placed anywhere within their designated proximal or distal (or both) dendritic sections (i.e. as in ***Guet-McCreight and Skinner (2018)***). For estimated numbers of X1 theta-timed excitatory inputs, we increased the number of inputs on either proximal or distal dendrites, until a large enough power spectral density (PSD) was obtained (i.e. 50 spikes^2/Hz). For estimated numbers of X1 theta-timed inhibitory inputs, we first increased a current input at the soma until a base spike rate of 35 Hz was attained. We then increased the number of inhibitory inputs on either proximal or distal dendrites until a large enough PSD was obtained (i.e. 80 spikes^2/Hz). Between the proximal and distal dendrites for the SDprox1 and SDprox2 models, we estimated approximately 27 synapses per excitatory presynaptic

population and approximately 8 synapses per inhibitory presynaptic population. Note that we used these same estimates for SWR-timed presynaptic populations.

Unless otherwise noted, presynaptic spiking for both theta-timed inputs and SWR-timed inputs were idealized, such that they spiked perfectly on time at their prescribed frequencies. For theta, this was 8 Hz for all presynaptic populations. For SWR inputs this varied across different populations (excitatory: 100 Hz, feedforward proximal inhibitory: 120 Hz, feedforward distal inhibitory: 20 Hz; ***Figure 5B***), and the duration was limited to 50 ms.

To simulate both theta-timed and SWR-timed inputs, we used NEURON's NetStim function to simulate spike trains with corresponding frequencies. For theta-timed inputs, we adjusted the start time of the presynaptic populations depending on their phase preferences. Finally, we also analyzed the effects of fractional randomness on theta-recruitment (***Figure 4***, ***Figure Supplement 2***). The fractional randomness (i.e. noise values between 0 and 1), controls the proportion by which each spike interval is influenced by the set interval value versus a random interval value sampled from a negative exponential distribution with a mean duration of noise × interval.

$$t_0 = (1 - noise) \times interval \tag{6}$$

$$\bar{t} = noise \times interval \tag{7}$$

$$f(t - t_0, \bar{t}) = \begin{cases} \frac{1}{\bar{t}} \times exp\left(\frac{-(t-t_0)}{\bar{t}}\right), & \text{if } t \geq t_0 \\ 0, & \text{if } t < t_0 \end{cases} \tag{8}$$

Where t is time, *interval* is the set inter-spike interval, and *noise* is the fractional randomness. This probability density function ensures that t_0 is the minimum possible interval, that the maximum possible interval is infinite, and that the mean expected interval is $(1-noise)\times interval + noise \times interval$. Here we found that theta-recruitment was optimal with a 0.01 level of fractional randomness (noise; ***Figure 4***, ***Figure Supplement 2***).

Short-term Plasticity

We decided not to explicitly model short term facilitation (i.e., a form of short-term plasticity, STP) as observed experimentally since we felt that we were already extrapolating enough from the existing data. Further, explicit data on STP for inhibitory synapses is not yet available to consider, and our *in vivo*-like representations were necessarily approximate (***Guet-McCreight and Skinner, 2018***). Also, since both pathways were found to be facilitating, it is unlikely that incorporating STP facilitation in our synaptic models would cause any major changes in the model output and predictions at this stage. Specifically, as we used just enough synapses for recruitment considerations and explorations (see 'theta-timed inputs' above), adding STP would likely just reduce the number of synapses needed for this. Also, the pre-synaptic frequencies may not be high enough to fully engage STP dynamics. For the models presented here, it is the relative contributions of different pathways and presynaptic inhibitory populations in considering IS3 cell recruitment given their morphological and biophysical characteristics together with a reasonable capturing of their relative synaptic properties (see ***Figure 3***) .

Stereotaxic injections

For *in vivo* two-photon calcium imaging, AAV1.Syn.Flex.GCaMP6f.WPRE.SV40 (Penn Vector Core) was injected in the CA1 area of VIP-Cre mice to express GCaMP6f selectively in VIP+ interneurons.

For stereotaxic injection, mice were deeply anaesthetized with intraperitoneal injection of ketamine–xylasine mixture (100 /10 mg kg^{-1}) and fixed on a stereotaxic frame (Kopf Instruments). Viral vector was delivered using a microprocessor-controlled nanoliter injector according to the following coordinates: CA1 (two sites were injected): site 1: AP - 2.5 mm, ML +2.1 mm, DV - 1.3

mm; site 2: AP, -2.0, ML, + 1.6, DV, -1.3 mm. Viral vector was injected with the speed of 1 mm/min. The total volume was 100 nl. The pipette was kept for 5 min after injection and then withdrawn slowly, and the scalp was sutured. After injection, mice were treated with a postoperative pain killer buprenorphine (0.1 mg/kg^{-1}; 48 h) for 3 consecutive days or buprenorphine slow release (0.1mg/kg^{-1}) once. Animals were recovered for 7-10 days before the implantation of hippocampal imaging window.

In vivo two-photon Ca2+-imaging in awake mice

Two-photon somatic Ca^{2+}-imaging of neuronal activity was performed simultaneously with contralateral local field potential (LFP) recording in head-fixed awake mice running on a treadmill. One week after viral injection, a glass-bottomed cannula was inserted on top of the dorsal hippocampus and secured with Kwik-Sil at the tissue interface and Superbond at the skull level (***Dombeck et al., 2010***). A single tungsten electrode (33 Ω–CM/F, California Fine Wire) for LFP recordings was implanted in the stratum pyramidale of the contralateral CA1 region and a reference electrode was implanted above the cerebellum (***Villette et al., 2017***). The head plate was oriented medio-laterally at 7–13° using a four-axis micromanipulator (MX10L, Siskiyou) and fixed with several layers of Superbond and dental cement. Mice were allowed to recover for several days with postoperative pain killer treatment for 3 consecutive days (buprenorphine, 0.1 mg/ kg^{-1}; 48 h).

The head fixation platform was described previously by ***Villette et al.*** (***2017***). Briefly, a head plate was clamped to a XY moveable metal frame, which minimized brain motion artifacts during recording. The treadmill was equipped with lateral walls to increase animal contentment and coupled with an optical encoder allowing for synchronous acquisition of running speed and electrophysiological signal. After recovery from surgery, animals were handled for 5-15 min twice per day for two days prior to the beginning of the experiment. During experiments, animals alternated between two behavior states: immobility and walking-running periods. The LFP signal and animal running speed were acquired at a sampling frequency of 10 kHz using the DigiData1440 (Molecular Devices), AM Systems amplifier and the AxoScope software (v10.5, Molecular Devices). Two-photon imaging was performed using a Leica SP5 TCS two-photon system coupled with a Ti:sapphire femtosecond laser (Chameleon Ultra II, Coherent), tuned to 900 nm. A long-range water-immersion 25× objective (0.95 NA, 2.5 mm working distance) was used for fluorophore excitation and light collection to external photomultiplier tubes at 12 bits. Image series were acquired at axial resolutions of 2 μm/pixel and temporal resolutions of 48 images/sec.

For each cell recorded, two 5-min imaging sessions were acquired. For each animal, the total length of imaging did not exceed 1 h. After imaging session, animals were returned to home cage. Between animals, the treadmill was cleaned with tap water. IS3 cells were identified post hoc using criteria described in the main text (***Figure 7***, ***Figure Supplement 1****A-B*, top).

Immunohistochemistry and morphological reconstructions

For immunohistochemical analysis of molecular markers expressed in hippocampal CA1, animals were intracardially perfused with sucrose ACSF followed by 4% paraformaldehyde (PFA), then the brain was extracted and fixed in 4% PFA overnight at 4 °C. On the next day, fixed brains were embedded in 4% agar. Hippocampal sections (thickness, 40–70 μm) were obtained using a vibratome (VT1000; Leica Microsystems or PELCO EasySlicer) and stored in PB sodium azide (0.5mg/ml) solution. Sections were permeabilized with 0.1–0.3% Triton X-100 in TBS or PBS and incubated in blocking solution containing 20% normal serum for 1 h. Then sections were incubated with primary antibodies at 4°C for 24–48 h. After that, slices were incubated with conjugated secondary antibodies for 2–4 h, rinsed, and mounted on microscope slides. Confocal images were obtained using a Leica TCS SP5 imaging system or Zeiss slide scanner (Axio Scan.Z1) equipped with a 488 nm argon, a 543 nm HeNe, or a 633 nm HeNe laser and a 20 × (NA 0.8), a 40 × (NA 1.4) or a 63 × (NA 1.4) oil-immersion objectives. The primary antibodies used were chicken-GFP (1:1000; Aves Labs Inc., Cat: GFP-1020), goat-CR (1:1000; Santa Cruz Biotechnology, Cat: 705-165-003),

rabbit-CCK (1:800; Sigma, Cat: C2581). The secondary antibodies used were: donkey anti chicken-Alexa Flour 488 (1:1000, Jackson Immunoresearch, Cat: 703-545-155), donkey anti goat-Dylight 650 (1:250; Thermo scientific, Cat: SA5-10089), donkey anti rabbit-Alexa Flour 647 (1:250; Invitrogen, Cat: A31573).

For post hoc mophological reconstruction, patched cells were filled with biocytin (0.6 mg/ml, Sigma) during patch-clamp recording. After recording, 300 μm-thick slices were fixed in 4% PFA at 4°C overnight. To reveal biocytin, the slices were permeabilized with 0.3% Triton X-100 and incubated at 4 °C with streptavidin-conjugated Alexa-488 (1:1000, Jackson Immunoresearch, Cat: 016-540-084) or Alexa-546 (1:1000, Invitrogen, Cat: S11225) in TBS. Z-stacks of biocytin-filled cells were acquired with a 1.5 μm step and merged for detailed reconstruction in Neurolucida 8.26.2 (MBF Bioscience).

Data analysis

Data acquired in electrophysiological experiments was analyzed in Clampfit 10.5 (Molecular Devices) and Igor Pro 4.0 (WaveMetrics). For the analysis of the AP properties, the first AP evoked with a current step of +40 to +60 pA within 50 ms from the beginning of the current step was analyzed. The AP amplitude was measured from the threshold to the peak. The AP half-width was measured at the voltage level corresponding to the half of the AP amplitude. Input resistance (Rin) and capacitance (Cm) were obtained using a membrane test in Clampex (Molecular Devices). The membrane time constant (τ) was measured offline using an exponential fit of voltage response during hyperpolarization with -100 pA current step in Clampfit 10.5 (Molecular Devices). Soma area, dendritic length and dendritic surface were generated automatically from the 3D reconstructions of recorded cells in Neurolucida 8.26.2.

For the analysis of speed traces, we looked at spontaneous time points as well as sustained periods. Spontaneous locomotion activity was defined as time points where the speed was greater than 1 cm/s. Immobility time points were defined as the times when the speed was less than 1 cm/s. The run epochs were defined similar to ***Fu et al.*** (***2014***), where we identified contiguous periods when the instantaneous speed was larger than 1 cm/s for a minimal time period of 3s (221 epochs of mean duration 8.95s $\pm$ 0.47 SEM). To identify run-starts for plotting in ***Figure 7B-D***, only run epochs where the average speed was below 1 cm/s for the 5s preceding them were selected (N = 64; 17/18 cells). Likewise, to identify run-stops, only run epochs where the average speed was below 1 cm/s in the 5s following them were selected (N = 69; 18/18 cells). Stationary epochs were defined as contiguous periods when the instantaneous speed was smaller than 1 cm/s for a minimal time period of 3s (556 epochs of mean duration 9.31s $\pm$ 0.31s SEM).

The image analysis was performed off-line using Leica LAS, Igor Pro (Wavemetrics, Lake Oswego, USA) and Matlab. For extraction of somatic Ca^{2+}-transients, a region of interest was drawn around individual soma to generate the relative fluorescence change (F) versus time trace. For the purposes of automating the analysis, the baseline fluorescence level (F0) was taken to be the median of Ca^{2+} signal. Somatic Ca^{2+}-transients were expressed as ΔF/F = (F - F0)/F0. This analysis was performed for 18 different pIS3 cells, of which 14 were recorded across two independent imaging sessions, which were separated by 1 min interval. Analyses between these sessions were pooled together for each cell. Cross-correlations were computed using Matlab's `xcorr(____,'coeff')` function.

To extract estimated spike times from Ca^{2+} events, we used three different methods. The first method was custom-written using Matlab, whereas the other two are previously developed algorithms, which were also available in Matlab. For the first method, we took the gradient of the calcium signal (DF/Dt), and chose times where the DF/Dt trace crosses a threshold value during the calcium signal onset (i.e. similar to ***Jackson et al.*** (***2016***)). For the threshold value, we used a moving threshold that depends on a normalized version of the amplitude of the raw calcium signal (i.e. calcium signal normalized to have values ranging from zero to one, or $\widehat{Ca}^{2+}_{Signal}$):

$$Threshold(t) = \left(\overline{\frac{dF}{dt}Ca^{2+}_{Signal}} + \left(\widehat{Ca}^{2+}_{Signal}(t) - 0.5\right)\right) \cdot \sigma_{\frac{dF}{dt}Ca^{2+}_{Signal}} + 2 \cdot \sigma_{\frac{dF}{dt}Ca^{2+}_{Signal}} \quad (9)$$

where the threshold at time *t*, depends on the normalized signal at time t ($\widehat{Ca}^{2+}_{Signal}(t)$), shifted to a value between -0.5 and 0.5, which is added to the mean of the DF/Dt of the calcium signal ($\overline{\frac{dF}{dt}Ca^{2+}_{Signal}}$) to produce a value above or below the mean, depending on whether the shifted normalized calcium signal is positive or negative. These time-dependent values are scaled by the standard deviation of the DF/Dt of the calcium signal ($\sigma_{\frac{dF}{dt}Ca^{2+}_{Signal}}$), and then shifted to a higher threshold value by adding 2 times the standard deviation of the DF/Dt of the calcium signal ($2 \cdot \sigma_{\frac{dF}{dt}Ca^{2+}_{Signal}}$) at each time point. We also added the condition that for any spike to be recognized, the corresponding data point in the processed calcium signal must be greater than 1.5 (similar to ***Jackson et al.*** (***2016***), though they use 0.15 instead). This adds accuracy for only identifying times that are during calcium events. While this method does a reasonable job at identifying periods of calcium signal onset, it is not as precise as the other two methods (see below).

Secondly, we used the UFARSA algorithm (Ultra-Fast Accurate Reconstruction of Spiking Activity) (***Rahmati et al., 2018***). While this algorithm appears to be much more selective in the spike time estimates, it is possible that it often under-estimated the number of spikes within a trace compared to the other methods used. This may be because it appears to only have been tested against calcium traces obtained using a synthetic Ca^{2+}-indicator Oregon-Green BAPTA-1. Because of this, we adjusted several internal parameters (***Table 2***) beyond their recommended values to increase the number of within-event spikes (though not to the point where its accuracy in identifying periods of calcium activation begins to drop).

Thirdly, we used the MLspike algorithm (***Deneux et al., 2016***), which we tuned to be optimal for GCaMP6f data, as well as the levels of noise seen in our calcium recordings (***Table 2***). To optimize the accuracy for each calcium trace, we used MLspike's functions for estimating the noise levels. While this algorithm was very good at identifying periods of calcium influx, it is possible that it over-estimated the number of spikes within these periods, compared to the other two methods used, given the parameters that we tuned it to. To generate spike rate traces from all spike estimation algorithms, we used a 2s sliding window time bin (resolution of 1s).

To examine somatic Ca^{2+}-fluctuations in relation to network oscillations, LFP traces were band-pass filtered in the forward and reverse directions to obtain theta-filtered (5–12 Hz, 4th order) or ripples-filtered (125–250 Hz, 8th order) signals in Matlab as follows:

```
[z,p,g] = butter(order,[min_frequency max_frequency]/nyquist,'bandpass');
[sos,g] = zp2sos(z,p,g);
filtered_signal = filtfilt(sos,g,LFP_signal);
```

The onset of the theta-run epoch, which was always associated with an increase in theta power, was defined by the beginning of the locomotion period based on the animal speed trace acquired simultaneously with LFP. To examine the time-varying relationships with theta power, we extracted the maximum powers from the spectrograms of the theta-filtered LFP traces between 5-12 Hz in Matlab, as follows:

```
window_theta = 20000;
overlap = [];
freqrange_theta = 0:0.001:20;
[s,f,t] = spectrogram(filtered_signal,window_theta,overlap,freqrange_theta,fs)
a = abs(s);
for l = 1:length(t)
    Theta_area(l) = max(a((f>5 & f<12),l));
end
```

We labeled periods where the time-varying theta power was greater than its mean as periods of "high-theta activity". For obtaining spike phases from the estimated spike times, we took the Hilbert transform (i.e. Matlab's `hilbert(____)` function) of the theta-filtered LFP signal and interpolated the spike phases from this trace. In this case, we set 0° to the rising phase of the theta oscillation.

Ripple events were detected automatically using custom-written Matlab code. Specifically, we

Table 2. Spike estimation algorithm parameters. Note that parameters that varied from their default parameter values are included in this table. Parameters and code statements are presented in the same chronological order as how they appear in the code. In particular UFARSA is run twice, the first time being to optimize the noise estimation parameter.

UFARSA	
Initial opt.scale_NoiseSTD	2.25
opt.remove_drifts	1
opt.remove_posDeflections	0
opt.remove_negDeflections	0
opt.demerging	1
output1	`[output1,~] = run_UFARSA(opt)`
Finding peaks	`pks = findpeaks(output1.fluors.afterSmoothing)`
Finding minimum peak	`Amp_min = min(pks(pks>(mean(pks)+2*std(pks))))`
Optimized opt.scale_NoiseSTD	`Amp_min/output1.std_noise`
output	`[output,~] = run_UFARSA(opt)`
UFARSA Internal Parameter Adjustments	
opt.scale_burstAmp	0.05
opt.scale_min_interior_thr	0.1
MLspike	
pax	`pax = spk_autosigma('par')`
pax.bias	1
Sigma Estimation	`sigmaest = spk_autosigma(catrace,dt,pax)`
par	`par = tps_mlspikes('par')`
par.a	0.0341
par.tau	0.76
par.pnonlin	[0.85, -0.0006]
par.finetune.sigma	`sigmaest`
par.drift.parameter	0.01
spikest	`[spikest,~,~] = spk_est(catrace,par)`

computed the envelope of the ripple-filtered trace by taking the absolute (`abs(____)`) of its Hilbert transform (`hilbert(____)`). We then set a threshold criteria to identify time periods where the envelope was greater than its mean plus 5 times its standard deviation for at least 12.5 ms. We chose this threshold criteria manually to ensure that ripple events were both large enough in amplitude and long enough in duration. These time periods were then marked as ripple periods.

Statistical analysis

Data was initially tested for normality using a Kolmogorov–Smirnov or Shapiro-Wilcoxon test. If data was normally distributed, standard parametric statistics such as one-way ANOVA were used (*$p < 0.05$, **$p < 0.01$, ***$p < 0.001$) to evaluate statistical significance. If data was not normally distributed, Dunn's test or Mann–Whitney test were used for comparisons of multiple groups. The data are presented as means $\pm$ SEM.

Statistical significance of cross-correlations were evaluated by doing a structured reshuffling of 10s segments of the speed traces or time-varying theta power traces to generate 1,000 surrogate cross-correlation traces. Within this surrogate dataset, the 95th and 99th percentile traces were computed using Matlab's `prctile(____)` function, in order to evaluate whether the peak or zeroth cross-correlation magnitudes fell above these percentiles.

We computed Pearson's linear correlation coefficient between the different spike rate estimates

and calcium signals using Matlab's `corr(X,Y,'Type','Pearson')` function. Note that this function was also used to compute Pearson's linear correlation coefficient between the calcium signals and speed traces. For comparisons of percent of normalized numbers of spikes between immobile and mobile states, we used Matlab's `ttest(x,y,'Alpha',__)` function, to perform paired-sample t-tests.

All circular statistical and descriptive measurements were computed using the CircStat toolbox in Matlab. Significance of the non-uniformity of circular spike estimate distributions relative to theta phase were tested using Rayleigh's method (`circ_rtest(____)`), and directional circular statistics were calculated using V-Tests (`circ_vtest(____)`). Mean theta-phase modulation of spike estimates were computed using the circular mean (`circ_mean(____)`) and measures of dispersion included the vector length (`circ_r(____)`) and the angular deviation (`circ_std(____)`).

Acknowledgments

This work was supported by the Canadian Institutes of Health Research (CIHR) and the Natural Sciences and Engineering Research Council of Canada (NSERC). Vincent Villette was supported by the PDF fellowship from Savoy Foundation. Alexandre Guet-McCreight was supported by an NSERC CGS-D2 award. We thank Sarah Côté for technical assistance and Dimitry Topolnik for equipment calibration and maintenance.

References

Acsády L, Arabadzisz D, Freund TF. Correlated morphological and neurochemical features identify different subsets of vasoactive intestinal polypeptide-immunoreactive interneurons in rat hippocampus. Neuroscience. 1996 Jul; 73(2):299–315. http://www.sciencedirect.com/science/article/pii/0306452295006109, doi: 10.1016/0306-4522(95)00610-9.

Acsády L, Görcs TJ, Freund TF. Different populations of vasoactive intestinal polypeptide-immunoreactive interneurons are specialized to control pyramidal cells or interneurons in the hippocampus. Neuroscience. 1996 Jul; 73(2):317–334. http://www.sciencedirect.com/science/article/pii/0306452295006095, doi: 10.1016/0306-4522(95)00609-5.

Ali AB, Deuchars J, Pawelzik H, Thomson AM. CA1 pyramidal to basket and bistratified cell EPSPs: dual intracellular recordings in rat hippocampal slices. The Journal of Physiology. 1998 Feb; 507(Pt 1):201–217. https://www.ncbi.nlm.nih.gov/pmc/articles/PMC2230771/, doi: 10.1111/j.1469-7793.1998.201bu.x.

Ali AB, Thomson AM. Facilitating pyramid to horizontal oriens-alveus interneurone inputs: dual intracellular recordings in slices of rat hippocampus. The Journal of Physiology. 1998 Feb; 507(Pt 1):185–199. https://www.ncbi.nlm.nih.gov/pmc/articles/PMC2230767/, doi: 10.1111/j.1469-7793.1998.185bu.x.

Amilhon B, Huh CYL, Manseau F, Ducharme G, Nichol H, Adamantidis A, Williams S. Parvalbumin Interneurons of Hippocampus Tune Population Activity at Theta Frequency. Neuron. 2015 Mar; 86(5):1277–1289. http://www.cell.com/article/S0896627315004341/abstract, doi: 10.1016/j.neuron.2015.05.027.

Andersen P, Morris R, Amaral D, Bliss T, O'Keefe J. The Hippocampus Book. Oxford Neuroscience Series, Oxford, New York: Oxford University Press; 2006.

Andrásfalvy BK, Magee JC. Distance-Dependent Increase in AMPA Receptor Number in the Dendrites of Adult Hippocampal CA1 Pyramidal Neurons. Journal of Neuroscience. 2001 Dec; 21(23):9151–9159. http://www.jneurosci.org/content/21/23/9151, doi: 10.1523/JNEUROSCI.21-23-09151.2001.

Antal M, Fukazawa Y, Eördögh M, Muszil D, Molnár E, Itakura M, Takahashi M, Shigemoto R. Numbers, Densities, and Colocalization of AMPA- and NMDA-Type Glutamate Receptors at Individual Synapses in the Superficial Spinal Dorsal Horn of Rats. Journal of Neuroscience. 2008 Sep; 28(39):9692–9701. http://www.jneurosci.org/content/28/39/9692, doi: 10.1523/JNEUROSCI.1551-08.2008.

Arrigoni E, Greene RW. Schaffer collateral and perforant path inputs activate different subtypes of NMDA receptors on the same CA1 pyramidal cell. British Journal of Pharmacology. 2004; 142(2):317–322. https://bpspubs.onlinelibrary.wiley.com/doi/abs/10.1038/sj.bjp.0705744, doi: 10.1038/sj.bjp.0705744.

Brandalise F, Carta S, Helmchen F, Lisman J, Gerber U. Dendritic NMDA spikes are necessary for timing-dependent associative LTP in CA3 pyramidal cells. Nature Communications. 2016 Nov; 7:13480. https://www.nature.com/articles/ncomms13480, doi: 10.1038/ncomms13480.

Carnevale NT, Hines ML. The NEURON Book. 1 edition ed. Cambridge, UK ; New York: Cambridge University Press; 2006.

Chamberlain SEL, Yang J, Jones RSG. The Role of NMDA Receptor Subtypes in Short-Term Plasticity in the Rat Entorhinal Cortex. Neural Plasticity. 2008; 2008. https://www.ncbi.nlm.nih.gov/pmc/articles/PMC2577183/, doi: 10.1155/2008/872456.

Chamberland S, Salesse C, Topolnik D, Topolnik L. Synapse-Specific Inhibitory Control of Hippocampal Feedback Inhibitory Circuit. Frontiers in Cellular Neuroscience. 2010; 4. https://www.frontiersin.org/articles/10.3389/fncel.2010.00130/full, doi: 10.3389/fncel.2010.00130.

Chamberland S, Topolnik L. Inhibitory control of hippocampal inhibitory neurons. Frontiers in Neuroscience. 2012; 6. https://www.frontiersin.org/articles/10.3389/fnins.2012.00165/full, doi: 10.3389/fnins.2012.00165.

Chatzikalymniou AP, Skinner FK. Deciphering the Contribution of Oriens-Lacunosum/Moleculare (OLM) Cells to Intrinsic Theta Rhythms Using Biophysical Local Field Potential (LFP) Models. eNeuro. 2018 Aug; p. ENEURO.0146–18.2018. http://www.eneuro.org/content/early/2018/08/22/ENEURO.0146-18.2018, doi: 10.1523/ENEURO.0146-18.2018.

Chen TW, Wardill TJ, Sun Y, Pulver SR, Renninger SL, Baohan A, Schreiter ER, Kerr RA, Orger MB, Jayaraman V, Looger LL, Svoboda K, Kim DS. Ultrasensitive fluorescent proteins for imaging neuronal activity. Nature. 2013 Jul; 499(7458):295–300. https://www.nature.com/articles/nature12354, doi: 10.1038/nature12354.

Chittajallu R, Wester JC, Craig MT, Barksdale E, Yuan XQ, Akgül G, Fang C, Collins D, Hunt S, Pelkey KA, McBain CJ. Afferent specific role of NMDA receptors for the circuit integration of hippocampal neurogliaform cells. Nature Communications. 2017 Jul; 8(1):152. https://www.nature.com/articles/s41467-017-00218-y, doi: 10.1038/s41467-017-00218-y.

Croce A, Pelletier JG, Tartas M, Lacaille JC. Afferent-specific properties of interneuron synapses underlie selective long-term regulation of feedback inhibitory circuits in CA1 hippocampus. The Journal of Physiology. 2010; 588(12):2091–2107. https://physoc.onlinelibrary.wiley.com/doi/abs/10.1113/jphysiol.2010.189316, doi: 10.1113/jphysiol.2010.189316.

David LS, Topolnik L. Target-specific alterations in the VIP inhibitory drive to hippocampal GABAergic cells after status epilepticus. Experimental Neurology. 2017 Jun; 292:102–112. http://www.sciencedirect.com/science/article/pii/S0014488617300687, doi: 10.1016/j.expneurol.2017.03.007.

Deneux T, Kaszas A, Szalay G, Katona G, Lakner T, Grinvald A, Rózsa B, Vanzetta I. Accurate spike estimation from noisy calcium signals for ultrafast three-dimensional imaging of large neuronal populations *in vivo*. Nature Communications. 2016 Jul; 7:12190. https://www.nature.com/articles/ncomms12190, doi: 10.1038/ncomms12190.

Dombeck DA, Harvey CD, Tian L, Looger LL, Tank DW. Functional imaging of hippocampal place cells at cellular resolution during virtual navigation. Nature Neuroscience. 2010 Nov; 13(11):1433–1440. https://www.nature.com/articles/nn.2648, doi: 10.1038/nn.2648.

Domonkos A, Ledri LN, Laszlovszky T, Cserép C, Borhegyi Z, Papp E, Nyiri G, Freund TF, Varga V. Divergent in vivo activity of non-serotonergic and serotonergic VGluT3–neurones in the median raphe region. The Journal of Physiology. 2016 Jul; 594(13):3775–3790. https://physoc.onlinelibrary.wiley.com/doi/abs/10.1113/JP272036, doi: 10.1113/JP272036.

Dragoi G, Carpi D, Recce M, Csicsvari J, Buzsáki G. Interactions between Hippocampus and Medial Septum during Sharp Waves and Theta Oscillation in the Behaving Rat. Journal of Neuroscience. 1999 Jul; 19(14):6191–6199. http://www.jneurosci.org/content/19/14/6191, doi: 10.1523/JNEUROSCI.19-14-06191.1999.

Dudman JT, Tsay D, Siegelbaum SA. A Role for Synaptic Inputs at Distal Dendrites: Instructive Signals for Hippocampal Long-Term Plasticity. Neuron. 2007 Dec; 56(5):866–879. http://www.sciencedirect.com/science/article/pii/S089662730700815X, doi: 10.1016/j.neuron.2007.10.020.

Emri Z, Antal K, Gulyás AI, Megias M, Freund TF. Electrotonic profile and passive propagation of synaptic potentials in three subpopulations of hippocampal CA1 interneurons. Neuroscience. 2001 Jul; 104(4):1013–1026. http://www.sciencedirect.com/science/article/pii/S0306452201001361, doi: 10.1016/S0306-4522(01)00136-1.

Ernst M, Brauchart D, Boresch S, Sieghart W. Comparative modeling of GABAA receptors: limits, insights, future developments. Neuroscience. 2003 Jul; 119(4):933–943. http://www.sciencedirect.com/science/article/pii/S0306452203002884, doi: 10.1016/S0306-4522(03)00288-4.

Francavilla R, Villette V, Luo X, Chamberland S, Munoz-Pino E, Camire O, Wagner K, Kis V, Somogyi P, Topolnik L. Connectivity and network state-dependent recruitment of long-range VIP-GABAergic neurons in the mouse hippocampus. bioRxiv. 2018 Jul; p. 364547. https://www.biorxiv.org/content/early/2018/07/15/364547, doi: 10.1101/364547.

Frerking M, Schulte J, Wiebe SP, Stäubli U. Spike Timing in CA3 Pyramidal Cells During Behavior: Implications for Synaptic Transmission. Journal of Neurophysiology. 2005 Aug; 94(2):1528–1540. http://jn.physiology.org/content/94/2/1528, doi: 10.1152/jn.00108.2005.

Freund TF, Gulyás AI, Acsády L, Görcs T, Tóth K. Serotonergic control of the hippocampus via local inhibitory interneurons. Proceedings of the National Academy of Sciences. 1990 Nov; 87(21):8501–8505. http://www.pnas.org/content/87/21/8501, doi: 10.1073/pnas.87.21.8501.

Fu Y, Tucciarone JM, Espinosa JS, Sheng N, Darcy DP, Nicoll RA, Huang ZJ, Stryker MP. A Cortical Circuit for Gain Control by Behavioral State. Cell. 2014 Mar; 156(6):1139–1152. https://www.cell.com/cell/abstract/S0092-8674(14)00144-5, doi: 10.1016/j.cell.2014.01.050.

Gillies MJ, Traub RD, LeBeau FEN, Davies CH, Gloveli T, Buhl EH, Whittington MA. A model of atropine-resistant theta oscillations in rat hippocampal area CA1. The Journal of Physiology. 2002 Sep; 543(Pt 3):779–793. https://www.ncbi.nlm.nih.gov/pmc/articles/PMC2290530/, doi: 10.1113/jphysiol.2002.024588.

Glickfeld LL, Scanziani M. Distinct timing in the activity of cannabinoid-sensitive and cannabinoid-insensitive basket cells. Nature Neuroscience. 2006 Jun; 9(6):807–815. https://www.nature.com/articles/nn1688, doi: 10.1038/nn1688.

Gloveli T, Dugladze T, Saha S, Monyer H, Heinemann U, Traub RD, Whittington MA, Buhl EH. Differential involvement of oriens/pyramidale interneurones in hippocampal network oscillations in vitro. The Journal of Physiology. 2005; 562(1):131–147. https://physoc.onlinelibrary.wiley.com/doi/abs/10.1113/jphysiol.2004.073007, doi: 10.1113/jphysiol.2004.073007.

Golding NL, Staff NP, Spruston N. Dendritic spikes as a mechanism for cooperative long-term potentiation. Nature. 2002 Jul; 418(6895):326–331. https://www.nature.com/articles/nature00854, doi: 10.1038/nature00854.

Guet-McCreight A, Camiré O, Topolnik L, Skinner FK. Using a Semi-Automated Strategy to Develop Multi-Compartment Models That Predict Biophysical Properties of Interneuron-Specific 3 (IS3) Cells in Hippocampus. eNeuro. 2016 Aug; 3(4). doi: 10.1523/ENEURO.0087-16.2016.

Guet-McCreight A, Luo X, Francavilla R, Topolnik L, Skinner FK. Using computational modeling to estimate synaptic receptor densities along hippocampal CA1 interneuron specific 3 cell dendrites (Poster). F1000Research. 2017 Aug; 6. https://f1000research.com/posters/6-1552, doi: 10.7490/f1000research.1114780.1.

Guet-McCreight A, Skinner FK. Weak and equally balanced synaptic inputs to interneurons in the CA1 hippocampus characterize in vivo rhythmic states. bioRxiv. 2018 Mar; p. 286369. https://www.biorxiv.org/content/early/2018/03/22/286369, doi: 10.1101/286369.

Gulyás AI, Hájos N, Freund TF. Interneurons Containing Calretinin Are Specialized to Control Other Interneurons in the Rat Hippocampus. Journal of Neuroscience. 1996 May; 16(10):3397–3411. http://www.jneurosci.org/content/16/10/3397.

Gulyás AI, Megias M, Emri Z, Freund TF. Total Number and Ratio of Excitatory and Inhibitory Synapses Converging onto Single Interneurons of Different Types in the CA1 Area of the Rat Hippocampus. Journal of Neuroscience. 1999 Nov; 19(22):10082–10097. http://www.jneurosci.org/content/19/22/10082.

Hainmüller T, Krieglstein K, Kulik A, Bartos M. Joint CP-AMPA and group I mGlu receptor activation is required for synaptic plasticity in dentate gyrus fast-spiking interneurons. Proceedings of the National Academy of Sciences. 2014 Sep; 111(36):13211–13216. http://www.pnas.org/content/111/36/13211, doi: 10.1073/pnas.1409394111.

Hangya B, Borhegyi Z, Szilágyi N, Freund TF, Varga V. GABAergic Neurons of the Medial Septum Lead the Hippocampal Network during Theta Activity. Journal of Neuroscience. 2009 Jun; 29(25):8094–8102. http://www.jneurosci.org/content/29/25/8094, doi: 10.1523/JNEUROSCI.5665-08.2009.

Helboe L, Egebjerg J, de Jong IEM. Distribution of serotonin receptor 5-HT6 mRNA in rat neuronal subpopulations: A double in situ hybridization study. Neuroscience. 2015 Dec; 310:442–454. http://www.sciencedirect.com/science/article/pii/S030645221500891X, doi: 10.1016/j.neuroscience.2015.09.064.

Jackson J, Ayzenshtat I, Karnani MM, Yuste R. VIP+ interneurons control neocortical activity across brain states. Journal of Neurophysiology. 2016 Jun; 115(6):3008–3017. http://jn.physiology.org/content/115/6/3008, doi: 10.1152/jn.01124.2015.

Katona L, Lapray D, Viney TJ, Oulhaj A, Borhegyi Z, Micklem BR, Klausberger T, Somogyi P. Sleep and Movement Differentiates Actions of Two Types of Somatostatin-Expressing GABAergic Interneuron in Rat Hippocampus. Neuron. 2014 May; 82(4):872–886. http://www.cell.com/neuron/abstract/S0896-6273(14)00297-9, doi: 10.1016/j.neuron.2014.04.007.

Katz B, Miledi R. The role of calcium in neuromuscular facilitation. The Journal of Physiology. 1968 Mar; 195(2):481–492. https://www.ncbi.nlm.nih.gov/pmc/articles/PMC1351674/.

Klausberger T, Magill PJ, Márton LF, Roberts JDB, Cobden PM, Buzsáki G, Somogyi P. Brain-state- and cell-type-specific firing of hippocampal interneurons in vivo. Nature. 2003 Feb; 421(6925):844–848. https://www.nature.com/nature/journal/v421/n6925/full/nature01374.html, doi: 10.1038/nature01374.

Klausberger T, Somogyi P. Neuronal Diversity and Temporal Dynamics: The Unity of Hippocampal Circuit Operations. Science. 2008 Jul; 321(5885):53–57. http://www.sciencemag.org/content/321/5885/53, doi: 10.1126/science.1149381.

Kullmann DM, Lamsa KP. Long-term synaptic plasticity in hippocampal interneurons. Nature Reviews Neuroscience. 2007 Sep; 8(9):687–699. https://www.nature.com/articles/nrn2207, doi: 10.1038/nrn2207.

Köhler C. Distribution and morphology of vasoactive intestinal polypeptide-like immunoreactive neurons in regio superior of the rat hippocampal formation. Neuroscience Letters. 1982 Dec; 33(3):265–270. http://www.sciencedirect.com/science/article/pii/0304394082903822, doi: 10.1016/0304-3940(82)90382-2.

Lamsa K, Irvine EE, Giese KP, Kullmann DM. NMDA receptor-dependent long-term potentiation in mouse hippocampal interneurons shows a unique dependence on Ca2+/calmodulin-dependent kinases. The Journal of Physiology. 2007; 584(3):885–894. https://physoc.onlinelibrary.wiley.com/doi/abs/10.1113/jphysiol.2007.137380, doi: 10.1113/jphysiol.2007.137380.

Lapray D, Lasztoczi B, Lagler M, Viney TJ, Katona L, Valenti O, Hartwich K, Borhegyi Z, Somogyi P, Klausberger T. Behavior-dependent specialization of identified hippocampal interneurons. Nature Neuroscience. 2012 Sep; 15(9):1265–1271. https://www.nature.com/neuro/journal/v15/n9/full/nn.3176.html, doi: 10.1038/nn.3176.

Le Roux N, Cabezas C, Böhm UL, Poncer JC. Input-specific learning rules at excitatory synapses onto hippocampal parvalbumin-expressing interneurons. The Journal of Physiology. 2013 Apr; 591(7):1809–1822. doi: 10.1113/jphysiol.2012.245852.

Lei S, McBain CJ. Distinct NMDA Receptors Provide Differential Modes of Transmission at Mossy Fiber-Interneuron Synapses. Neuron. 2002 Mar; 33(6):921–933. http://www.sciencedirect.com/science/article/pii/S0896627302006086, doi: 10.1016/S0896-6273(02)00608-6.

Leão RN, Mikulovic S, Leão KE, Munguba H, Gezelius H, Enjin A, Patra K, Eriksson A, Loew LM, Tort ABL, Kullander K. OLM interneurons differentially modulate CA3 and entorhinal inputs to hippocampal CA1 neurons. Nature Neuroscience. 2012 Nov; 15(11):1524–1530. https://www.nature.com/articles/nn.3235, doi: 10.1038/nn.3235.

Losonczy A, Zhang L, Shigemoto R, Somogyi P, Nusser Z. Cell type dependence and variability in the short-term plasticity of EPSCs in identified mouse hippocampal interneurones. The Journal of Physiology. 2002 Jul; 542(Pt 1):193–210. https://www.ncbi.nlm.nih.gov/pmc/articles/PMC2290398/, doi: 10.1113/jphysiol.2002.020024.

Lovett-Barron M, Kaifosh P, Kheirbek MA, Danielson N, Zaremba JD, Reardon TR, Turi GF, Hen R, Zemelman BV, Losonczy A. Dendritic Inhibition in the Hippocampus Supports Fear Learning. Science. 2014 Feb; 343(6173):857–863. http://science.sciencemag.org/content/343/6173/857, doi: 10.1126/science.1247485.

Lovett-Barron M, Turi GF, Kaifosh P, Lee PH, Bolze F, Sun XH, Nicoud JF, Zemelman BV, Sternson SM, Losonczy A. Regulation of neuronal input transformations by tunable dendritic inhibition. Nature Neuroscience. 2012 Mar; 15(3):423–430. https://www.nature.com/articles/nn.3024, doi: 10.1038/nn.3024.

Léránth C, Frotscher M, To¨mbo¨l T, Palkovits M. Ultrastructure and synaptic connections of vasoactive intestinal polypeptide-like immunoreactive non-pyramidal neurons and axon terminals in the rat hippocampus. Neuroscience. 1984 Jun; 12(2):531–542. http://www.sciencedirect.com/science/article/pii/030645228490071X, doi: 10.1016/0306-4522(84)90071-X.

Madisen L, Zwingman TA, Sunkin SM, Oh SW, Zariwala HA, Gu H, Ng LL, Palmiter RD, Hawrylycz MJ, Jones AR, Lein ES, Zeng H. A robust and high-throughput Cre reporting and characterization system for the whole mouse brain. Nature Neuroscience. 2010 Jan; 13(1):133–140. https://www.nature.com/articles/nn.2467, doi: 10.1038/nn.2467.

Magee JC, Cook EP. Somatic EPSP amplitude is independent of synapse location in hippocampal pyramidal neurons. Nature Neuroscience. 2000 Sep; 3(9):895–903. https://www.nature.com/articles/nn0900_895, doi: 10.1038/78800.

Masugi-Tokita M, Tarusawa E, Watanabe M, Molnár E, Fujimoto K, Shigemoto R. Number and Density of AMPA Receptors in Individual Synapses in the Rat Cerebellum as Revealed by SDS-Digested Freeze-Fracture Replica Labeling. Journal of Neuroscience. 2007 Feb; 27(8):2135–2144. http://www.jneurosci.org/content/27/8/2135, doi: 10.1523/JNEUROSCI.2861-06.2007.

Mizuseki K, Sirota A, Pastalkova E, Buzsáki G. Theta Oscillations Provide Temporal Windows for Local Circuit Computation in the Entorhinal-Hippocampal Loop. Neuron. 2009 Oct; 64(2):267–280. http://www.cell.com/neuron/abstract/S0896-6273(09)00673-4, doi: 10.1016/j.neuron.2009.08.037.

Nusser Z. A new approach to estimate the number, density and variability of receptors at central synapses. European Journal of Neuroscience. 1999; 11(3):745–752. https://onlinelibrary.wiley.com/doi/abs/10.1046/j.1460-9568.1999.00535.x, doi: 10.1046/j.1460-9568.1999.00535.x.

Nusser Z, Cull-Candy S, Farrant M. Differences in Synaptic GABAA Receptor Number Underlie Variation in GABA Mini Amplitude. Neuron. 1997 Sep; 19(3):697–709. http://www.sciencedirect.com/science/article/pii/S0896627300803827, doi: 10.1016/S0896-6273(00)80382-7.

Nyíri G, Stephenson FA, Freund TF, Somogyi P. Large variability in synaptic n-methyl-d-aspartate receptor density on interneurons and a comparison with pyramidal-cell spines in the rat hippocampus. Neuroscience. 2003 Jun; 119(2):347–363. http://www.sciencedirect.com/science/article/pii/S030645220300157X, doi: 10.1016/S0306-4522(03)00157-X.

Otmakhova NA, Otmakhov N, Lisman JE. Pathway-Specific Properties of AMPA and NMDA-Mediated Transmission in CA1 Hippocampal Pyramidal Cells. Journal of Neuroscience. 2002 Feb; 22(4):1199–1207. http://www.jneurosci.org/content/22/4/1199, doi: 10.1523/JNEUROSCI.22-04-01199.2002.

Papp EC, Hájos N, Acsády L, Freund TF. Medial septal and median raphe innervation of vasoactive intestinal polypeptide-containing interneurons in the hippocampus. Neuroscience. 1999 Feb; 90(2):369–382. http://www.sciencedirect.com/science/article/pii/S0306452298004552, doi: 10.1016/S0306-4522(98)00455-2.

Paul A, Crow M, Raudales R, He M, Gillis J, Huang ZJ. Transcriptional Architecture of Synaptic Communication Delineates GABAergic Neuron Identity. Cell. 2017 Oct; 171(3):522–539.e20. doi: 10.1016/j.cell.2017.08.032.

Pi HJ, Hangya B, Kvitsiani D, Sanders JI, Huang ZJ, Kepecs A. Cortical interneurons that specialize in disinhibitory control. Nature. 2013 Nov; 503(7477):521–524. https://www.nature.com/articles/nature12676, doi: 10.1038/nature12676.

Pinto L, Dan Y. Cell-Type-Specific Activity in Prefrontal Cortex during Goal-Directed Behavior. Neuron. 2015 Jul; 87(2):437–450. http://www.sciencedirect.com/science/article/pii/S0896627315005644, doi: 10.1016/j.neuron.2015.06.021.

Pouille F, Scanziani M. Routing of spike series by dynamic circuits in the hippocampus. Nature. 2004 Jun; 429(6993):717–723. https://www.nature.com/articles/nature02615, doi: 10.1038/nature02615.

Price CJ, Cauli B, Kovacs ER, Kulik A, Lambolez B, Shigemoto R, Capogna M. Neurogliaform Neurons Form a Novel Inhibitory Network in the Hippocampal CA1 Area. Journal of Neuroscience. 2005 Jul; 25(29):6775–6786. http://www.jneurosci.org/content/25/29/6775, doi: 10.1523/JNEUROSCI.1135-05.2005.

Prisco GVD, Albo Z, Vertes RP, Kocsis B. Discharge properties of neurons of the median raphe nucleus during hippocampal theta rhythm in the rat. Experimental Brain Research. 2002 Aug; 145(3):383–394. https://link.springer.com/article/10.1007/s00221-002-1123-8, doi: 10.1007/s00221-002-1123-8.

Rahmati V, Kirmse K, Holthoff K, Kiebel SJ. Ultra-fast accurate reconstruction of spiking activity from calcium imaging data. Journal of Neurophysiology. 2018 Feb; 119(5):1863–1878. https://www.physiology.org/doi/abs/10.1152/jn.00934.2017, doi: 10.1152/jn.00934.2017.

Regehr WG, Tank DW. Postsynaptic NMDA receptor-mediated calcium accumulation in hippocampal CAl pyramidal cell dendrites. Nature. 1990 Jun; 345(6278):807–810. https://www.nature.com/articles/345807a0, doi: 10.1038/345807a0.

Royer S, Zemelman BV, Losonczy A, Kim J, Chance F, Magee JC, Buzsáki G. Control of timing, rate and bursts of hippocampal place cells by dendritic and somatic inhibition. Nature Neuroscience. 2012 May; 15(5):769–775. https://www.nature.com/articles/nn.3077, doi: 10.1038/nn.3077.

Sambandan S, Sauer JF, Vida I, Bartos M. Associative Plasticity at Excitatory Synapses Facilitates Recruitment of Fast-Spiking Interneurons in the Dentate Gyrus. Journal of Neuroscience. 2010 Sep; 30(35):11826–11837. http://www.jneurosci.org/content/30/35/11826, doi: 10.1523/JNEUROSCI.2012-10.2010.

Shigemoto R, Kulik A, Roberts JDB, Ohishi H, Nusser Z, Kaneko T, Somogyi P. Target-cell-specific concentration of a metabotropic glutamate receptor in the presynaptic active zone. Nature. 1996 Jun; 381(6582):523–525. https://www.nature.com/articles/381523a0, doi: 10.1038/381523a0.

Sik A, Penttonen M, Ylinen A, Buzsaki G. Hippocampal CA1 interneurons: an in vivo intracellular labeling study. Journal of Neuroscience. 1995 Oct; 15(10):6651–6665. http://www.jneurosci.org/content/15/10/6651, doi: 10.1523/JNEUROSCI.15-10-06651.1995.

Silver RA. Neuronal arithmetic. Nature Reviews Neuroscience. 2010 Jul; 11(7):474–489. https://www.nature.com/articles/nrn2864, doi: 10.1038/nrn2864.

Siwani S, França ASC, Mikulovic S, Reis A, Hilscher MM, Edwards SJ, Leão RN, Tort ABL, Kullander K. OLMa2 Cells Bidirectionally Modulate Learning. Neuron. 2018 Jul; 99(2):404–412.e3. doi: 10.1016/j.neuron.2018.06.022.

Spruston N, Jonas P, Sakmann B. Dendritic glutamate receptor channels in rat hippocampal CA3 and CA1 pyramidal neurons. The Journal of Physiology. 1995 Jan; 482(Pt 2):325–352. https://www.ncbi.nlm.nih.gov/pmc/articles/PMC1157732/.

Stuart G, Spruston N. Determinants of Voltage Attenuation in Neocortical Pyramidal Neuron Dendrites. Journal of Neuroscience. 1998 May; 18(10):3501–3510. http://www.jneurosci.org/content/18/10/3501, doi: 10.1523/JNEUROSCI.18-10-03501.1998.

Sun HY, Dobrunz LE. Presynaptic Kainate Receptor Activation Is a Novel Mechanism for Target Cell-Specific Short-Term Facilitation at Schaffer Collateral Synapses. Journal of Neuroscience. 2006 Oct; 26(42):10796–10807. http://www.jneurosci.org/content/26/42/10796, doi: 10.1523/JNEUROSCI.2746-06.2006.

Sun HY, Lyons SA, Dobrunz LE. Mechanisms of target-cell specific short-term plasticity at Schaffer collateral synapses onto interneurones versus pyramidal cells in juvenile rats. The Journal of Physiology. 2005; 568(3):815–840. https://physoc.onlinelibrary.wiley.com/doi/abs/10.1113/jphysiol.2005.093948, doi: 10.1113/jphysiol.2005.093948.

Swanson GT, Kamboj SK, Cull-Candy SG. Single-Channel Properties of Recombinant AMPA Receptors Depend on RNA Editing, Splice Variation, and Subunit Composition. Journal of Neuroscience. 1997 Jan; 17(1):58–69. http://www.jneurosci.org/content/17/1/58, doi: 10.1523/JNEUROSCI.17-01-00058.1997.

Szabo A, Somogyi J, Cauli B, Lambolez B, Somogyi P, Lamsa KP. Calcium-Permeable AMPA Receptors Provide a Common Mechanism for LTP in Glutamatergic Synapses of Distinct Hippocampal Interneuron Types. Journal of Neuroscience. 2012 May; 32(19):6511–6516. http://www.jneurosci.org/content/32/19/6511, doi: 10.1523/JNEUROSCI.0206-12.2012.

Thomson AM. Activity-dependent properties of synaptic transmission at two classes of connections made by rat neocortical pyramidal axons in vitro. The Journal of Physiology. 1997 Jul; 502(Pt 1):131–147. https://www.ncbi.nlm.nih.gov/pmc/articles/PMC1159577/.

Tyan L, Chamberland S, Magnin E, Camiré O, Francavilla R, David LS, Deisseroth K, Topolnik L. Dendritic Inhibition Provided by Interneuron-Specific Cells Controls the Firing Rate and Timing of the Hippocampal Feedback Inhibitory Circuitry. Journal of Neuroscience. 2014 Mar; 34(13):4534–4547. http://www.jneurosci.org/content/34/13/4534, doi: 10.1523/JNEUROSCI.3813-13.2014.

Unal G, Joshi A, Viney TJ, Kis V, Somogyi P. Synaptic Targets of Medial Septal Projections in the Hippocampus and Extrahippocampal Cortices of the Mouse. Journal of Neuroscience. 2015 Dec; 35(48):15812–15826. http://www.jneurosci.org/content/35/48/15812, doi: 10.1523/JNEUROSCI.2639-15.2015.

Varga C, Golshani P, Soltesz I. Frequency-invariant temporal ordering of interneuronal discharges during hippocampal oscillations in awake mice. Proceedings of the National Academy of Sciences. 2012 Oct; 109(40):E2726–E2734. http://www.pnas.org/content/109/40/E2726, doi: 10.1073/pnas.1210929109.

Varga C, Oijala M, Lish J, Szabo GG, Bezaire M, Marchionni I, Golshani P, Soltesz I. Functional fission of parvalbumin interneuron classes during fast network events. eLife. 2014 Nov; 3:e04006. https://elifesciences.org/articles/04006, doi: 10.7554/eLife.04006.

Villette V, Levesque M, Miled A, Gosselin B, Topolnik L. Simple platform for chronic imaging of hippocampal activity during spontaneous behaviour in an awake mouse. Scientific Reports. 2017 Feb; 7:43388. https://www.nature.com/articles/srep43388, doi: 10.1038/srep43388.

Viney TJ, Lasztoczi B, Katona L, Crump MG, Tukker JJ, Klausberger T, Somogyi P. Network state-dependent inhibition of identified hippocampal CA3 axo-axonic cells *in vivo*. Nature Neuroscience. 2013 Dec; 16(12):1802–1811. https://www.nature.com/articles/nn.3550, doi: 10.1038/nn.3550.

Wang DV, Yau HJ, Broker CJ, Tsou JH, Bonci A, Ikemoto S. Mesopontine median raphe regulates hippocampal ripple oscillation and memory consolidation. Nature Neuroscience. 2015 May; 18(5):728–735. https://www.nature.com/articles/nn.3998, doi: 10.1038/nn.3998.

Wyskiel DR, Andrade R. Serotonin excites hippocampal CA1 GABAergic interneurons at the stratum radiatum-stratum lacunosum moleculare border. Hippocampus. 2016 Sep; 26(9):1107–1114. https://onlinelibrary.wiley.com/doi/abs/10.1002/hipo.22611, doi: 10.1002/hipo.22611.

Zucker RS, Regehr WG. Short-Term Synaptic Plasticity. Annual Review of Physiology. 2002; 64(1):355–405. https://doi.org/10.1146/annurev.physiol.64.092501.114547, doi: 10.1146/annurev.physiol.64.092501.114547.

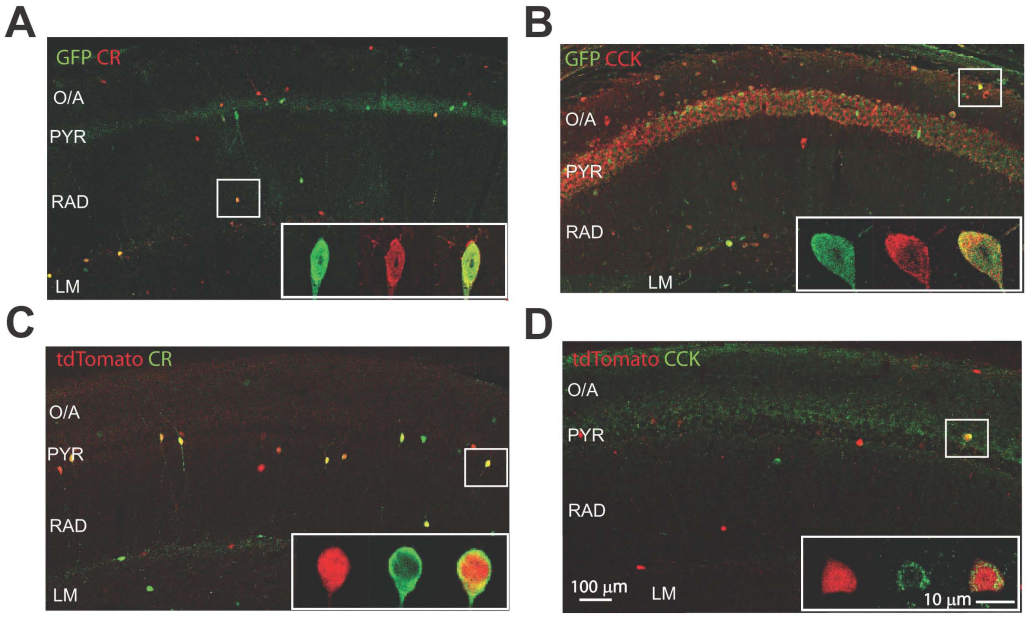

Figure 1–Figure supplement 1. Immunolabelling for CR and CCK in the CA1 hippocampal area of VIP-eGFP (green) and VIP-tdTomato (red) mice. A-B: GFP (green), CR (red) and CCK (red) immunoreactivity is shown overlayed. Insets in the lower right corner delineated by a white frame show examples of cells co-expressing GFP and CR (A) or GFP and CCK (B). **C-D:** tdTomato (red), CR (green) and CCK (green) immunolabelling overlayed. Insets in the lower right corner delineated by a white frame show examples of cells co-expressing tdTomato and CR (C) or tdTomato and CCK (D).

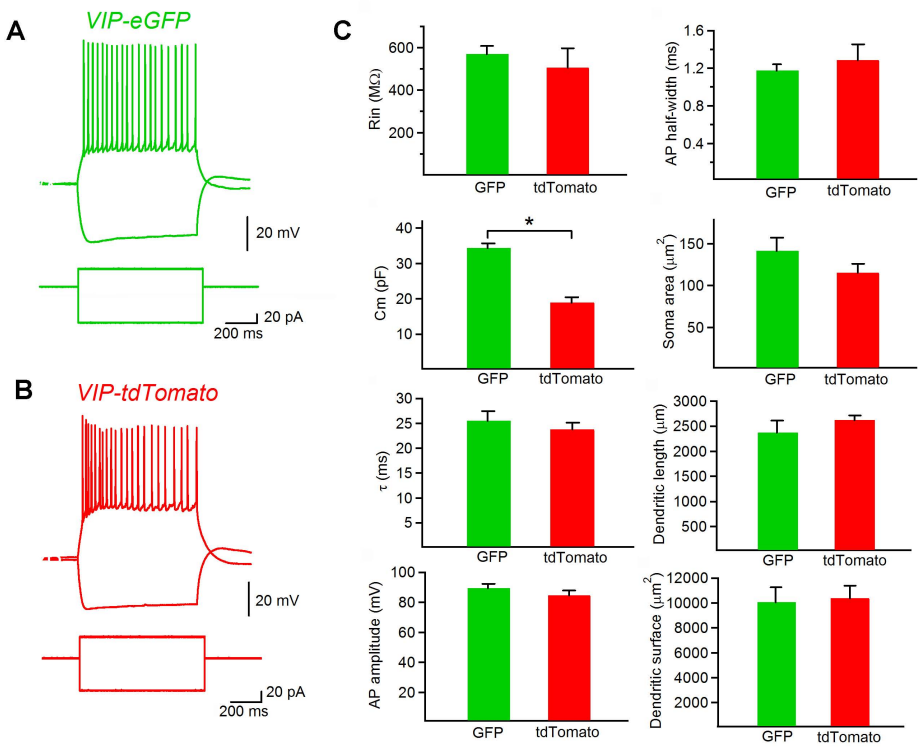

Figure 1–Figure supplement 2. Membrane and morphological properties of IS3 cells in VIP-eGFP (green) and VIP-tdTomato (red) mouse lines. **A-B:** Example traces of voltage responses (top) to depolarizing and hyperpolarizing current steps (bottom). **C:** Comparison of membrane properties and morphological parameters of IS3 cells in VIP-eGFP (green) and VIP-tdTomato (red) mouse lines.

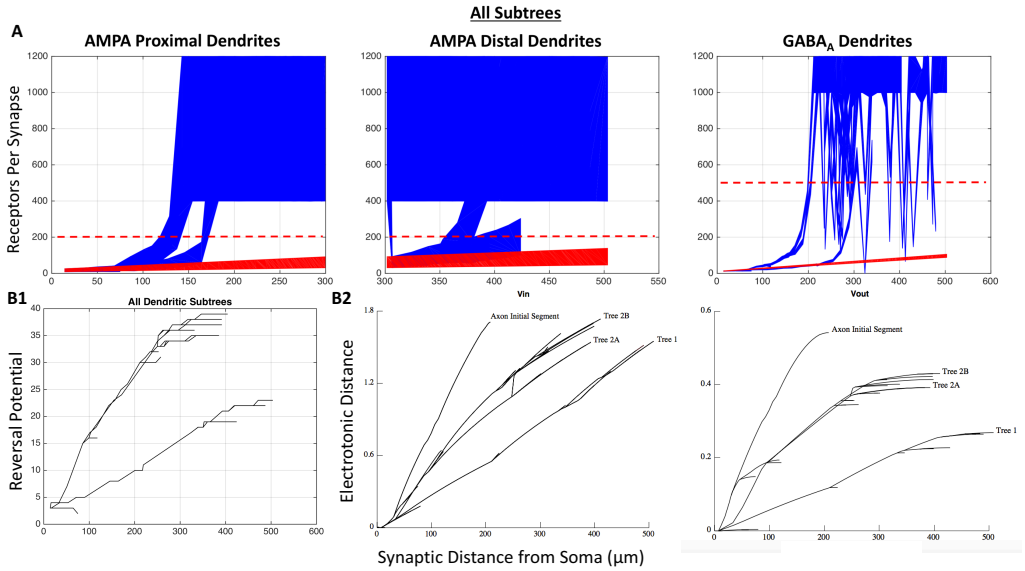

Figure 3–Figure supplement 1. Receptor numbers, reversal potentials and electrotonic distances. A: Predicted ranges of receptors per synapse, calculated based on the fitted weights (blue) and the linearly rectified distance-dependent weights (red). Note that each x-axis data point shows a range which is larger or smaller depending on the thickness (along the y-axis) of the plotted line. Dashed red line denotes the maximal limits as per previous findings from other cell types in the literature. Line bifurcations in this plot correspond to bifurcations in the dendritic morphology. **B1:** Estimated reversal potential of each synapse along the dendritic arbor of the model using a simulated protocol that is similar to what is used experimentally. Note that the true reversal potential of each excitatory synapse is 0 mV, and does not change during these simulations. Line bifurcations in this plot correspond to bifurcations in the dendritic morphology. **B2:** Electrotonic distance (i.e. decay of a 1 mV signal) for voltage flowing into the soma (left) and voltage flowing out of the soma (right). Note that the subtree organization approximately follows the same organization as in B1, suggesting that reversal potential recordings in IS3 cells are sensitive to distance-dependent voltage decay.

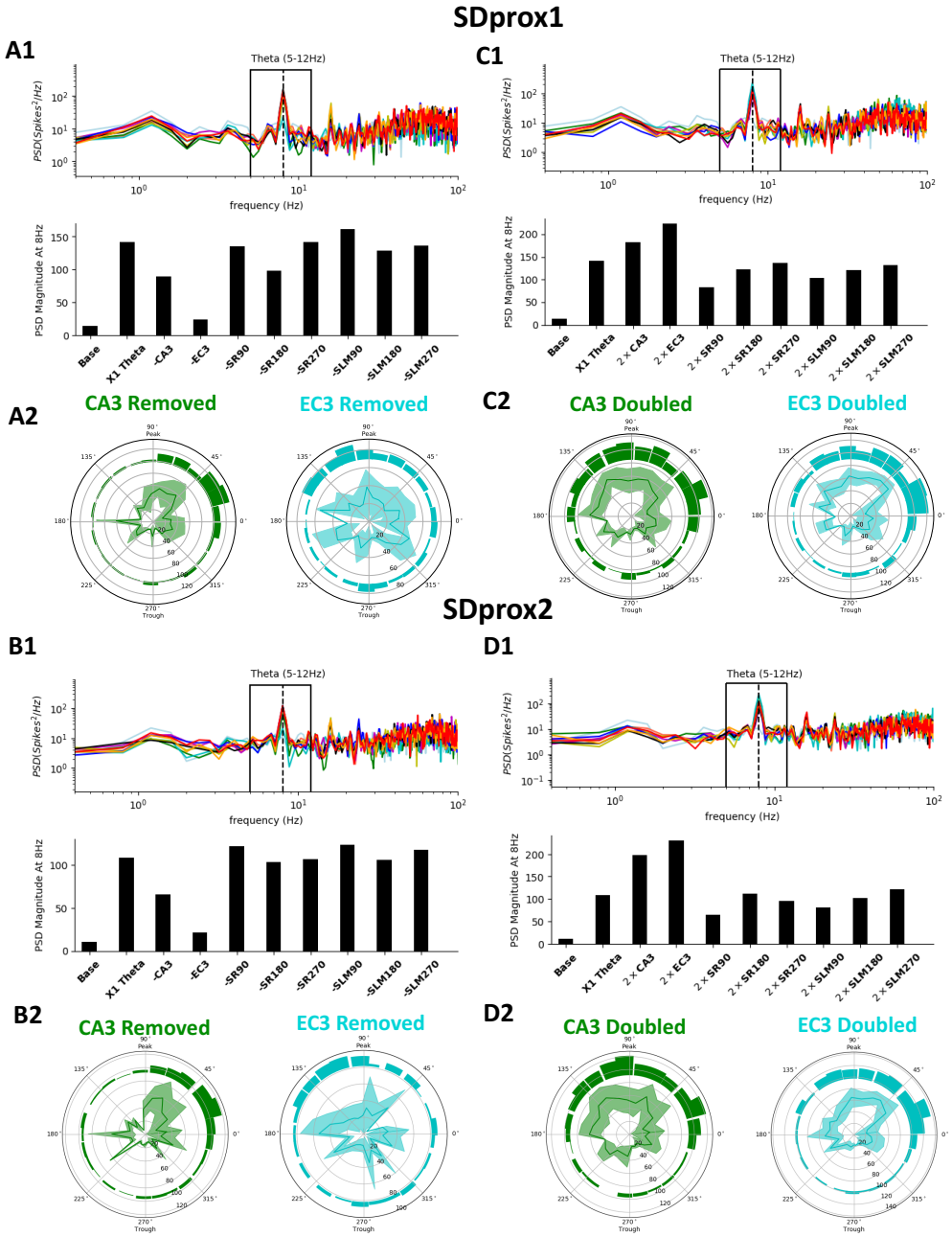

Figure 4–Figure supplement 1. Excitatory presynaptic populations can modulate timing of IS3 cell spikes during theta rhythms. A1-B1: Same as in Figure 4*C* for X1 theta-timed inputs, but during removal of specified presynaptic theta-timed populations. Bottom subplots show only the PSD at 8 Hz. **A2-B2:** Same as in the Figure 4*D* theta polar plots (bin width = 14.4°), but during removal of either CA3 or EC3. **C-D:** Same as in A-B, but with doubled presynaptic populations instead of removed. Acronyms: CA3 - Cornu Ammonis 3, EC3 - Entorhinal Cortex Layer 3, SR90/180/270 - Theta Peak/Falling Phase/Trough -Timed Proximal Inhibition, SLM90/180/270 - Theta Peak/Falling Phase/Trough -Timed Distal Inhibition.

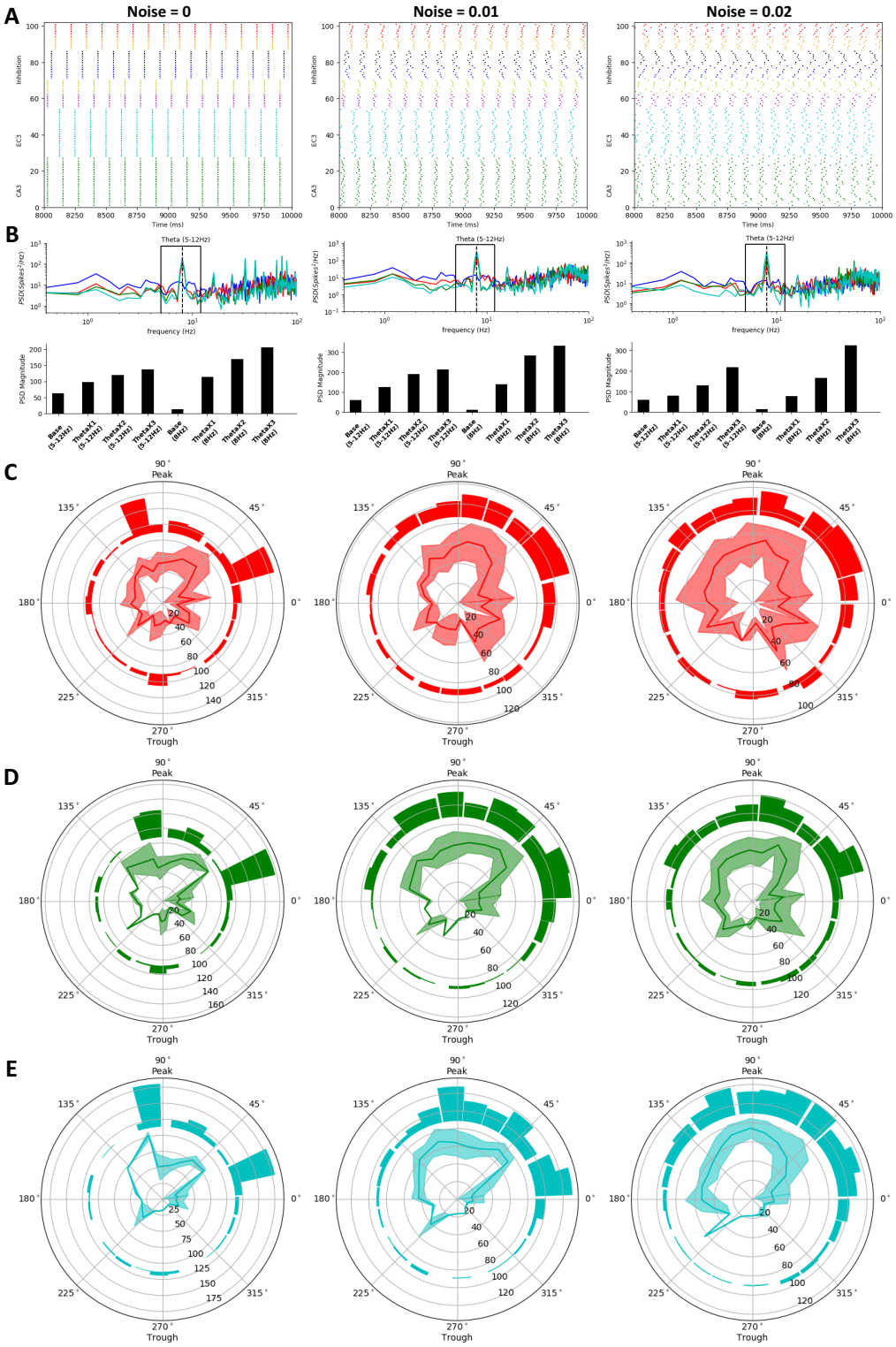

Figure 4–Figure supplement 2. Effect of fractional randomness (noise) on theta-recruitment in the SDprox1 model. **A:** Example X1 theta raster plots of the presynaptic theta-timed populations. **B:** Same as in Figure 4*C*. **C-E:** Polar plots (same as in Figure 4*D*) showing phase preference of the IS3 cell model for X1 (C), X2 (D), and X3 (E) theta inputs (bin width = 14.4°).

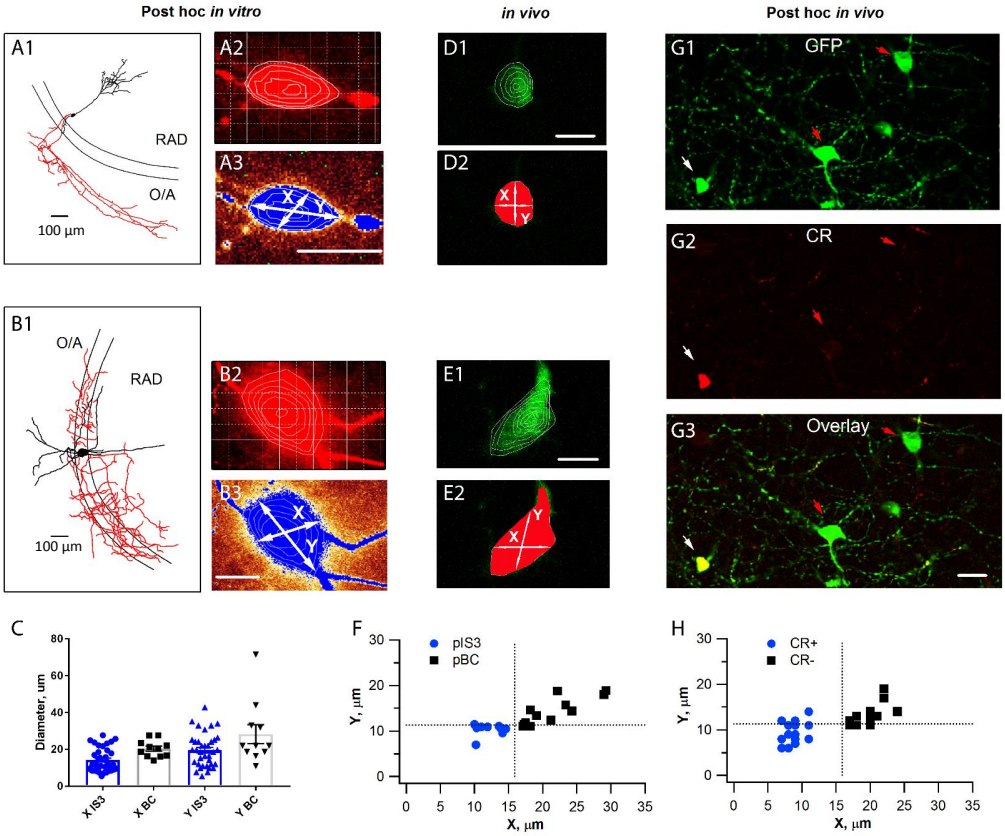

Figure 6–Figure supplement 1. Morphological criteria used for the VIP cell identification. A-B: Neurolucida 3D reconstructions (A1, B1) and confocal images (A2-A3, B2-B3; maximal projections of 10–32 sections) illustrating the analysis of somatic parameters in anatomically confirmed IS3 cells and BCs filled during in vitro patch-clamp recordings with biocytin. 3D rendering of somatic surface (A2, B2) was used to derive somatic diameters in medio-lateral (X-axis) and rostro-caudal (Y-axis) dimensions (A3, B3). **C:** Summary bar graphs illustrating the distributions of somatic diameters in a group of cells (IS3, blue, n = 36; BC, black, n = 11). **D-E:** Two-photon raw (D1, E1) and mask (D2, E2) images of VIP interneurons recorded in vivo showing the extraction of somatic X- and Y-parameters for cell identification. **F:** Summary data showing the clustering of in vivo recorded VIP cells based on the distribution of X- and Y-parameters (pIS3, blue, n = 9; pBC, black, n = 12). Dotted lines indicate the cut-off levels obtained from in vitro analysis and used for in vivo cell segregation (X = 15.9 µm, Y = 11.3 µm). **G**: Representative confocal images of horizontal hippocampal sections processed for post hoc immunohistochemical identification following in vivo two-photon experiments illustrating the expression of GFP (G1), CR (G2) and both (G3). **H:** Summary group data showing the clustering of CR+ and CR- VIP cells based on the distribution of X- and Y-parameters (pIS3, blue, n = 17; pBC, black, n = 13). Dotted lines indicate the same cut-off levels.

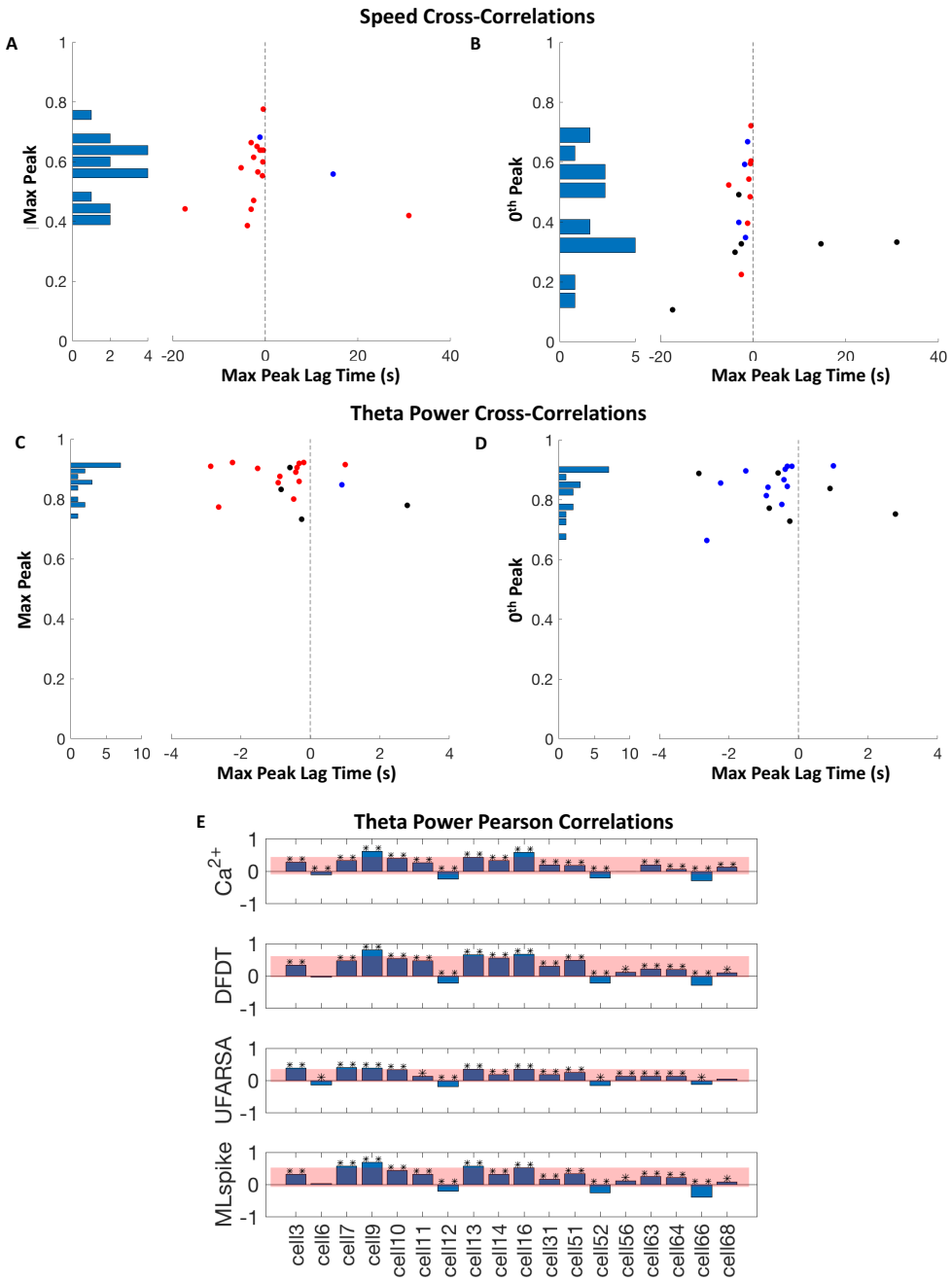

Figure 7–Figure supplement 1. Summary statistics of cross-correlations and Pearson correlations between theta power and calcium signal. A-B: Analysis of speed x calcium signal cross-correlations (for raw traces, see **Figure 7***E*). Dots indicate the lag time of the maximum peaks versus the magnitude of the maximum (A) or zeroth (B) peaks seen in the cross-correlations. Histograms along the ordinate axes show the distributions of cross-correlation maximum peak amplitudes and zeroth peak amplitudes. The color of dots indicates the significance of the cross-correlation using a 10s structured reshuffling surrogate analysis. Black dots indicate p-value > 0.05, blue dots indicate p-value < 0.05, and red dots indicate p-value < 0.01. **C-D:** Same as A-B but for analysis of theta power x calcium signal cross-correlations (for raw traces, see **Figure 7***F*). **E:** Same as in **Figure 7***G* but with time-varying theta power instead of speed.